

THESIS FOR THE DEGREE OF LICENTIATE OF PHILOSOPHY

Towards the Characterization of Biological Nanoparticles

SILVER JÕEMETSA



CHALMERS

Department of Physics

CHALMERS UNIVERSITY OF TECHNOLOGY

Göteborg, Sweden 2018

Towards the Characterization of Biological Nanoparticles

SILVER JÕEMETSA

© SILVER JÕEMETSA, 2018

Department of Physics
Chalmers University of Technology
SE-412 96 Gothenburg
Sweden
Telephone + 46 (0)31-772 1000

Printed at Chalmers Reproservice
Göteborg, Sweden 2018

Cover illustration: *Caricature of measuring a malicious but cute biological nanoparticle. (Margit Saal & Silver Jõemetsa, 2018)*

Abstract

Lipids are integral to all forms of life. Both cells and the majority of particles involved with living systems are enveloped by a lipid membrane, which protects their content from the external environment while simultaneously controlling molecular transport using membrane-embedded proteins. A subset of these particles are known as biological nanoparticles (BNPs), including extracellular vesicles, exosomes and viruses. BNPs are known to transfer genetic material during cellular communication, but many aspects of the mechanisms regulating their various functions remain unknown. Progress within this scientific discipline is hampered by their small size (between 50 and 200 nm in diameter) and significant biomolecular heterogeneity, making both quantitative nanoparticle analytics and functional characterization, highly demanding tasks.

To overcome the challenges of BNP characterization, we constructed an approach to identify the mechanism by which lipid vesicles are spontaneously converted into a planar supported lipid bilayer (SLB) on glass surfaces (Paper I). Total internal reflection fluorescence (TIRF) microscopy was used to track and temporally resolve the rate of vesicle adsorption, the onset of supported lipid bilayer (SLB) formation and the kinetics of their growth into a continuous SLB, through the use of a small fraction (1/100) of labelled lipid vesicles. It was found that the SLB formation processes was initiated by the merger of multiple small SLB patches at appreciably high vesicle coverage. In addition, the subsequent growth of SLB patches was, for the first time, shown to occur via a gradual increase in the average front velocity. Paper II focuses on quantifying both the size and molecular content of different types of BNPs. This was accomplished by tethering BNPs of varying complexity, to a fluid SLB formed on the floor of a microfluidic channel. By moving the BNPs with an applied hydrodynamic shear flow and by determining both the Brownian and directed motion using single particle tracking analysis, it was possible to determine the hydrodynamic radii for each BNP. Furthermore, imaging the BNPs using TIRF or epi-microscopy, made it possible to simultaneously determine the extent of fluorescent label attachment, which was specifically used to address how the incorporation efficiency of the membrane-staining dye spDIO depends on the size of the BNP.

The insights gained on the SLB formation processes and BNP characterization are fundamental for the future development and advancement of novel techniques aimed at probing the molecular interaction between BNPs and cellular membranes.

Keywords: supported lipid bilayer, TIRF microscopy, diffusion, size determination, lipophilic dyes, microfluidics

Appended Papers

Paper I

Spatiotemporal Kinetics of Supported Lipid Bilayer Formation on Glass via Vesicle Adsorption and Rupture

Mokhtar Mapar, Silver Jõemetsa, Hudson Pace, Vladimir P. Zhdanov, Björn Agnarsson, and Fredrik Höök

The Journal of Physical Chemistry Letters **2018** 9 (17), 5143-5149

My contribution: I planned and performed part of the experiments, prepared the figures. I was extensively involved in the data analysis and writing process.

Paper II

Membrane-Curvature Dependence of Self-inserted Dyes into Lipid Vesicles and Biological Nanoparticles

Silver Jõemetsa, Quentin Lubart, Mokhtar Mapar, Paul Joyce, Stephan Block, Marta Bally, Gavin D.M. Jeffries, and Fredrik Höök

In manuscript

My contribution: I planned and performed the experiments, analyzed the data, prepared the figures, and wrote the main part of the manuscript.

Abbreviations

2DFN	two-dimensional (2D) flow nanometry
BNP	biological nanoparticle
DLS	dynamic light scattering
EM	electron microscopy
EV	extracellular vesicle
FCM	flow cytometry
HSV1	Herpes Simplex type 1 virus
MSD	mean squared displacement
NMV	native membrane vesicle
NTA	nanoparticle tracking analysis
PDMS	poly-(dimethylsiloxane)
POPC	1-palmitoyl-2-oleoyl-sn-glycero-3-phosphocholine
Rh-PE	1,2-dioleoyl-sn-glycero-3-phosphoethanolamine-N-(lissamine rhodamine B sulfonyl) (ammonium salt)
SLB	supported lipid bilayer
spDIO	3,3'-Dioctadecyl-5,5'-Di(4-Sulfophenyl)Oxcarbocyanine
SUV	small unilamellar vesicle
TIRF	total internal reflection fluorescence

Table of Contents

Introduction.....	1
1 Background	5
1.1 Phospholipids and self-assembly	5
1.2 Vesicles and supported lipid bilayers	7
1.2.1 Formation techniques of SLBs	8
1.3 Biological Nanoparticles.....	9
1.3.1 Viruses	10
1.3.2 Extracellular vesicles.....	11
1.3.3 Native membrane vesicles.....	12
2 Nanoparticle Analytics	13
3 Experimental Methods	16
3.1 Total Internal Reflection Fluorescence Microscopy.....	16
3.2 Microfluidics.....	19
3.3 Size Determination.....	19
3.3.1 Nanoparticle Tracking Analysis	20
3.3.2 2D Flow Nanometry	22
4 Results	29
4.1 Paper I	29
4.2 Paper II.....	31
5 Future outlook	33
5.1 Size and intensity correlation of complex BNPs	33
5.2 High throughput device.....	34
5.3 Concentration determination.....	35
5.4 Native drug-delivery vehicles	38
6 Acknowledgements	39
References.....	41

Introduction

“The oldest and strongest emotion of mankind is fear, and the oldest and strongest kind of fear is fear of the unknown.” – H. P. Lovecraft

Life is a complex interplay of various physical and chemical processes that are integral to maintaining life, facilitating growth and preventing disease. Debilitating and fatal diseases that exist without a cure threaten this balance and consequently our well-being, be it cancer, viral infection or neurodegenerative disorders, such as Alzheimer’s disease (AD). AD is an increasingly common, fatal and incurable neurodegenerative disorder that causes impairments in memory and intellectual function of about approximately 50 million people worldwide [1]. Current treatment methods employed to treat AD are capable of suppressing symptoms and slowing the progression of the disease, but for such techniques to be effective, early identification and diagnosis is paramount. Since the biggest cost for AD comes from continued patient support and care once the disease has already progressed, there is an urgent need for the development of new technologies that are capable of detecting the disease prior to symptoms being prevalent. It is hypothesized that precise and sensitive BNP analysis techniques may contribute to improved detection for AD, since this will facilitate enhanced understanding of their role in the disease and direct the design of novel diagnostic tools.

One of the common factors involved in these diseases are small, nano-sized objects of biological origin, called biological nanoparticles (BNPs). Many of these particles are enveloped by a lipid membrane, thus sharing similarities with the host cell’s plasma membrane. This membrane, containing various phospholipids, proteins and carbohydrates, protects the internal content from the external environment. BNPs are responsible for a multitude of functions in the body, ranging from the aforementioned pathological conditions such as viral infection [2] to intercellular communication [3]. Furthermore, these BNPs have been proven to be natural and effective carriers of bioactive molecules, such as miRNA, mRNA, DNA, lipids, and proteins. This combination of a biocompatible envelope with the ability to carry bioactive cargo makes them an attractive target as or inspiration for drug delivery carriers.

Extracellular vesicles (EVs) constitute one example of such vessels, excreted from every cell type into body fluids such as plasma, urine and saliva [4]. They are highly heterogeneous

and believed to be involved in the progression and infection steps of a multitude of diseases, such as cancer [5] and different neurological conditions [4,6]. For instance, EVs may be involved in transferring proteins associated with AD between cells, thus causing accumulation and aggregation of protein in otherwise healthy cells [6]. There are also recent findings suggesting that various viruses are transmitted as viral cargo inside EVs [7,8]. Consequently, their abundance and involvement in various biological processes makes EVs relevant as diagnostic biomarkers. In order to gain insight on how they contribute to the development of disease, as well as cellular function, it is of relevance to investigate the huge compositional heterogeneity of BNP, which would enable their future use both as diagnostic biomarkers or novel therapeutic delivery vehicles. However, the combination of nano-scale size (typically 50 to 200 nm in diameter) and high molecular heterogeneity makes the characterization of these nanoparticles rather difficult [9].

This thesis work puts focus on the use and development of a new nanoparticle size determination tool that in addition to size of BNP, has been shown capable of determining both molecular content [10] and deformation [11] when propelled using a hydrodynamic force after being tethered to a mobile supported lipid bilayer (BNP). In order for the particles to move unobstructed, a defect-free highly reproducible supported lipid bilayer (SLB) is essential. To achieve this goal, total internal reflection fluorescence (TIRF) microscopy was used to monitor the kinetics of vesicle adsorption and subsequent rupture into individual lipid patches on planar surfaces with the objective to gain insight on the mechanism of SLB formation (Paper I). The types of SLBs investigated in Paper I, were in Paper II used as a two-dimensional fluid interface, to which BNPs of varying complexities were tethered, with the aim to address how the incorporation efficiency of dyes depends on the size of BNPs. More specifically, it has been the aim of this thesis work to compare artificial lipid vesicles, native-membrane vesicles and the enveloped virus HSV1; however, the majority of experiments that so far succeeded were designed to address how the incorporation efficiency of the membrane-staining dye spDIO compare with lipid-based dyes for synthetic vesicles.

The objective of this thesis is to provide the foundation for the experimental and analytical work leading up to the results presented in the appended papers. Specifically, Chapter 1 discusses lipid vesicles, SLBs and BNPs in more detail. Chapter 2 gives an overview of the most commonly used nanoparticle characterization tools for BNPs listing their unique strengths and limitations with an emphasis on size determination. Chapter 3 includes the principles for the methods used in this research with an emphasis on two-dimensional flow nanometry.

Chapter 4 summarizes and discusses the results of the appended papers. Finally, Chapter 5 concludes this thesis with an outlook for future and ongoing research plans.

1 Background

1.1 Phospholipids and self-assembly

Lipids are amphiphilic molecules that are characterized by a unique molecular structure comprised of a hydrophilic (polar) head-group attached to hydrophobic (non-polar) alkyl chains or ‘tail-groups’[12]. Lipids are essential to all forms of life and the functional properties of each is controlled by the chemical nature of their head-group and the length, number and saturation of the tail groups [13].

Of significant interest are phospholipids (phosphoglycerides), which are the main constituents of biological cell membranes and are, thus, essential for regulating cellular processes, function and health [14,15]. The plasma membrane constitutes a two-dimensional medium made up of a phospholipid bilayer, in which many different biological molecules, such as for example transmembrane proteins, are dissolved in. Owing to its unique structure, the cell membrane acts as a protective vessel for cell organelles separating the intracellular and extracellular spaces, while its semi-permeable properties facilitate transport of specific nutrients and waste products into and out of the cell [16]. The latter function, which is crucial for cellular communication, depends critically on key proteins and lipids that are embedded within the phospholipid bilayer.

Phospholipids are structurally comprised of two fatty acid groups linked to a glyceryl backbone [17]. Unlike other lipids such as triglycerides, the final glycerol hydroxyl group is replaced for a phosphate head-group, rather than a fatty acid chain (Figure 1). In biological membranes, hydrocarbon tails typically contain 10 to 18 carbons per chain, which are linked together by single bonds (saturated) or double bonds (unsaturated).

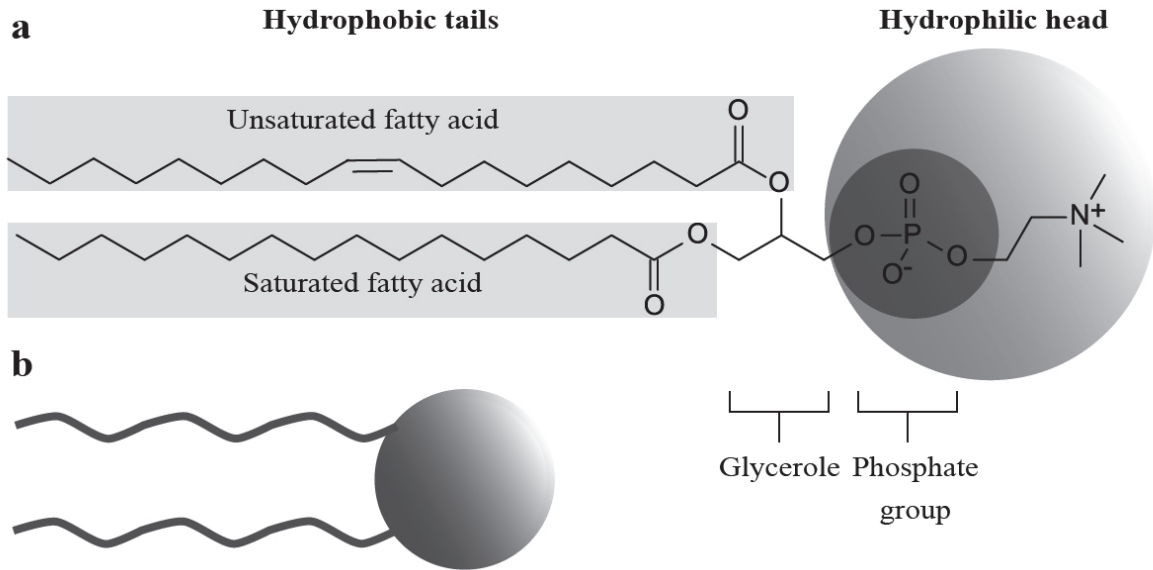


Figure 1. (a) Schematic representation of the phospholipid molecule POPC depicting the polar head-group, non-polar tail-groups, fatty acid chain saturation and additional chemical units. (b) A simplified illustration of a phospholipid.

To minimize the free energy when dispersed in an aqueous solution, the hydrophilic head of lipids screen the hydrophobic tails by spontaneously forming aggregates, referred to as the “hydrophobic effect” [18]. The spontaneous organization process of lipids (and other amphiphiles) from a disordered state to an ordered or semi-ordered arrangement is a thermodynamically driven process referred to as “self-assembly”. Exposure of water molecules to the non-polar component of lipid molecules contributes a reduction in H-bonding between water molecules [19]. If the hydrophobic molecule is small, water molecules salvage the lost H-bonds by forming cages that envelope the molecule without terminating any bonds, known as “hydrophobic solvation”. However, this interaction between water molecules near a hydrophobic interface is highly thermodynamically unfavorable, because the newly formed configurations have an increased degree of order, which in turn corresponds to a reduction in entropy. All systems strive towards increasing the entropy and thereby contributing to minimizing the Gibbs free energy (ΔG) of the system, given by:

$$\Delta G = \Delta H - T\Delta S, \quad 1.1.1$$

where ΔH is the change in enthalpy and $T\Delta S$ is the change in entropy. It should be noted that for a spontaneous process, such as self-assembly, to occur, the change in free energy ΔG must be < 0 . Despite the self-assembly of lipid molecules into an organized lipid membrane contributes to a lowering of the entropy, the overall entropy increases ($\Delta S > 0$) due

to release of ordered water around the hydrophobic tails, and accordingly the free energy is reduced. It should also be noted that the change in enthalpy (ΔH) is negligible compared to the $T\Delta S$ term [20]. Hence, lipid molecules spontaneously self-assemble into various organized structures in aqueous media in order to ‘hide’ their hydrophobic tails.

The type and geometries of colloidal structures formed by lipid molecules is determined by the effective head-group area, critical chain-length and hydrocarbon volume of the lipids [13]. This can be stipulated by relating the shape of the amphiphile to the critical packing parameter (CPP):

$$CPP = \frac{V}{AL}, \quad 1.1.2$$

where V is the volume taken by the hydrophobic (tail) part, A is the effective surface area of the head-group and L is the length of the tail-group. Single-chained lipids with bulky head-groups, defined by $CPP < 0.5$, such as the common detergent sodium dodecyl sulfate (SDS), tend to form micelles; phospholipids with two tails and a fairly large head-group, defined by $0.5 < CPP < 1$ tend to form bilayers and vesicles; and lipids with large hydrophobic tails, defined by $CPP > 1$, prefer to form reverse crystal phases, such as inverted micelles [20]. Most phospholipids have a cylindrical shape *i.e.* $CPP \sim 1$, and therefore tend to form lipid bilayer structures. As the edge of such bilayer structures are energetically unfavorable, they tend to adopt a closed spherical shape that encapsulates an aqueous volume inside the membrane, often named lipid vesicles or liposomes. However, the CPP and consequently the geometry of the self-assembled lipid based structure depends on numerous parameters, such as electrolyte and lipid concentration, pH or temperature, as they will influence the interactions between the lipid aggregates and also the intermolecular forces within each aggregate.

1.2 Vesicles and supported lipid bilayers

Colloidal structures composed of lipids arranged within a lamellar or bilayer structure are commonly referred to as lipid vesicles or liposomes. Vesicles may be artificially created or naturally occurring and are typically classified according to their size and number of bilayers. That is, vesicles may be classified as small (10-100 nm), large (100-1000 nm) and giant vesicles (larger than 1 μm), and as either uni- or multi-lamellar. The hydrophobic interior of lipid bilayers is a relatively homogeneous region of hydrocarbon chains, whereas the exterior comprises of the hydrophilic head-groups, which orient towards the aqueous medium. The

bilayer sheets are held together by hydrophobic interactions, the unusually strong entropically driven attraction between non-polar molecules, or regions, in water [20,21].

In order to gain insights into cellular processes and activities that are fundamental for cell survival, considerable research focus has, in recent decades, been directed towards analyzing the molecular interactions in and between lipid bilayer membranes. However, an overall lack of experimental techniques suitable for detailed investigations of such interactions has made progress relatively slow. One attractive approach to investigate key biophysical features of biological cell plasma membranes that meets the requirements of many high-end analytical tools is to use supported lipid bilayers (SLBs). Such SLBs are excellent model systems that retain two-dimensional fluidity, while providing reduced complexity and greater stability for the lipid membrane compared with cell membranes. This 2D membrane fluidity is believed to be maintained by a 10–20 Å layer of trapped water between the substrate and the bilayer [22–24]. This is also one reason why SLBs can harness the power of surface-specific and sensitive analytical techniques to derive novel insights into cellular membranes *e.g.* atomic force microscopy [25], fluorescence microscopy [26], quartz crystal microbalance, surface plasmon resonance [27] among others [28]. However, owing to the reduced complexity, it is crucial to well-characterize these native membrane mimics to accurately represent the appropriate membrane function for a specific application. Thus, significant efforts have been invested to characterize the formation mechanism under various conditions [29–34]. In this thesis work, the SLB formation process on borosilicate glass was investigated in paper I. SLBs are also excellent environments to incorporate linker molecules such as cholesterol-DNA in order to study binding [35] or even use the same SLB-linker system to preserve and study the mobility of tethered NPs [36]. This system was used in Paper II with various BNPs tethered to a fluid SLB to gain insight on their properties.

1.2.1 Formation techniques of SLBs

Under certain conditions, it is possible to adsorb lipid vesicles onto surfaces, and thus convert them into SLBs with a typical thickness of 4 to 5 nanometers (Figure 2). The ability to do so is dependent on temperature, properties of the lipid vesicles, the ionic strength of the surrounding solution and the properties of the surface [32]. In order to form SLBs with low defect density and high mobility, the surface should be hydrophilic, smooth and clean [37].

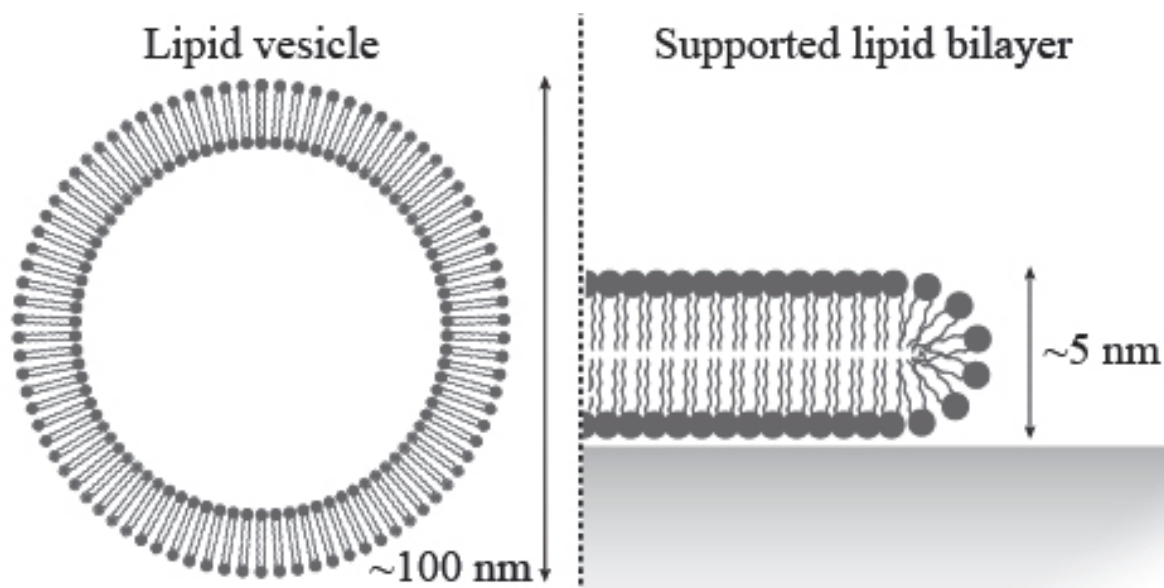


Figure 2. The cross-section of a vesicle (left). A supported lipid bilayer (right).

The historically predominant methods for surface deposition of lipid bilayers were Langmuir–Blodgett (LB) and Langmuir-Schaefer (LS) [34,38], while more recent methods include solvent-assisted lipid deposition [39] and a method where freeze-thawing is used to induce vesicle rupture and subsequent SLB formation [40]. The most popular SLB formation method, which was also used in this thesis work, is the adsorption and fusion of vesicles [41,42] on silica-rich surfaces such as borosilicate glass. In this case, vesicles approach the surface via diffusion from the bulk and adsorb if the surface-vesicle interaction is favorable. Although vesicles can occasionally rupture into small bilayer patches at a relatively low vesicle coverage, the SLB formation is initiated when a fairly high vesicle coverage is reached, after which they start to rupture into small patches that initiate growth and the auto-catalytic SLB formation cascade [27]. In Paper I, the aforementioned observations were investigated in detail by following the growth kinetics of individual SLB patches from the adsorption and rupture of vesicles.

1.3 Biological Nanoparticles

Biological nanoparticles (BNPs), such as extracellular vesicles, exosomes and viruses are involved in a multitude of key biological processes, including cellular communication and viral infection; the detailed molecular mechanisms of which are not yet understood. Accordingly, the characterization of BNPs and their associated processes has recently emerged as a focus area for the improved understanding of fundamental processes that control cellular health. Furthermore, BNPs have been proven to be natural and effective carriers of various bioactive

molecules, such as mRNA, DNA and proteins within the membrane envelope. Therefore, insights derived from investigations directed towards BNPs can be harnessed for biomimetic development of novel therapeutic delivery vehicles.

1.3.1 Viruses

Viruses are complex molecular machines capable of infecting all cellular life. Virus particles vary considerably in size and shape, ranging from 20 nm to 400 nm in diameter. Genetic viral material, composed of either DNA or RNA, is encapsulated within a protein capsid, which protects the genome from the extracellular environment. The protein capsid is in many cases enclosed within a lipid membrane that is derived from the outer plasma membrane of host cells or from one of the inner cellular membranes. As viruses are small nano-machines that are incapable of self-replication, they ‘hijack’ the replication machinery of cells by attaching and penetrating the cellular membrane and mixing their genetic material with the host cells genome [43]. In doing so, replication of the viral genome is facilitated and consequently the host cell is turned into a virus factory. Some viruses can even lead to permanent genetic changes of infected cells, leading to the development of cancer and other debilitating diseases [44].

In this thesis work, the membrane-enveloped herpes simplex virus type 1 (HSV1) was investigated with respect to the dependence on membrane staining as a function of virus size. Based on recent estimates, HSV1 has infected over 67% of the global population [45], and is believed to enter their host cells through fusion between its viral envelope and the plasma membrane, whereby the host cell is usually killed in the viral replication process [46]. Virus attachment is mediated by specific glycoproteins on the surface of the virus, which bind to receptors/sugar molecules on the cell surface [47], facilitating transmission of HSV1 between the host cells. Since the viral entry is mediated by membrane fusion through the binding of protein ligands to cell-surface receptors, this opens up a possibility to monitor virus binding to cell membrane mimics (see section 1.2) combined with advanced surface-based characterization techniques (see section 2) that can effectively monitor this process. As previously discussed, fluorescent microscopy techniques enables single-vesicle tracking of BNPs bound to supported cell-membrane mimics, given that HSV1 have been successfully labelled with suitable fluorophores, such as yellow-fluorescent protein (YFP) by genome modification [48]. However, this modification may affect the virus. Furthermore, the labelling efficiency and spatial distribution of YFP is only assumed to be constant and reproducible. Therefore, in this study, we have used an alternative labeling method, by directly targeting the

viral membrane using spDIO [49] and in Paper II the foundations for being able to investigate the labeling efficiency versus virus dimension.

1.3.2 Extracellular vesicles

Extracellular vesicles (EVs) are cell-secreted vesicles capable of carrying different cargo, such as lipids, proteins, DNA, mRNA and miRNA and are present in all body fluids [4,50]. These nanovesicles have been identified to play an important role in a variety of biological processes, including pathological conditions such as cancer and different neurological conditions, and have even been proposed to represent a common route for transport of neurodegenerative disease-related proteins and nucleic acids [6]. Specifically, transfer of proteins via exosomes from diseased cells to healthy cells frequently leads to accumulation and aggregation of the protein in the target cell, which is linked to the pathogenesis of many neurodegenerative diseases, such as Alzheimer's [6].

EVs are heterogeneous both in size and composition, with sizes ranging from 40 nm to 1 μm [51]. EVs include distinct subtypes such as exosomes, microvesicles and oncosomes (released by cancer cells) [52]. Exosomes, containing miRNA and mRNA, have been shown to transfer the genetic content which upon delivery can be translated to proteins by the receiving cells [53]. There are also reports suggesting that EVs can in fact spread viral cargo such as HSV1 in their envelope, which can be taken up by healthy cells, leading to viral infection [7]. Furthermore, studies have demonstrated that EV release kinetics from cancer cells varies considerably compared with healthy cells [5]. Therefore, EVs serve as promising biomarkers for a multitude of debilitating diseases and may also guide the development of novel therapeutic delivery systems based on their mode of action.

Consequently, in order to determine how these BNPs mediate biological processes and how EV malfunctioning contributes to the development of neurodegenerative and other diseases, there is a need to develop effective bioanalytical tools for improved analysis. Despite the existence of several bioanalytical tools for investigations of single nanoparticles, which will be introduced in the next chapter, precise determination of both size and content of each individual EV is rather difficult [9]. Preliminary measurements of EVs size distribution employing 2DFN (see section 3.3.2) and a high-throughput nanodevice [54] are ongoing, with more in-depth discussion provided in the Future Outlook section.

1.3.3 Native membrane vesicles

Since exosomes vary in composition, based on the producer cell type [55], and exhibit complex structures that are difficult to characterize, simpler systems are helpful for the development of new single nanoparticle analytical tools. Native membrane vesicles (NMVs) are one such simplified BNP systems that can be produced *in vitro* from the plasma membrane of a cell, while retaining the membrane components of the parent cell: lipids, proteins, carbohydrates [56,57]. Hence, the membrane of NMVs mimics closely the membrane composition of exosomes, since it is also derived from the host cell in which it was released from [6,58]. However, unlike exosomes, NMVs are easy to harvest from host cells with several simple ultracentrifugation steps [56], while still acting as a more closely related exosome model compared to synthetic vesicles. These simpler, native BNP were in this thesis work utilized as a model system that acted as a precursor for exosome characterization. Specifically, it was the intention to compare the size determination of NMVs with that of HSV1 and synthetic vesicles.

2 Nanoparticle Analytics

As mentioned in the previous chapter, a multitude of quantitative methods exist to characterize BNP properties, especially size. The predominant technique for the last few decades to gain insight on particle properties has been electron microscopy. However, certain limitations, especially with respect to cumbersome sample preparation, low throughput and high costs, have called for the development of complementary techniques. We will herein give an overview of these most commonly used BNP characterization methods (Table 1).

The traditionally used standard for single particle analytical techniques is considered to be electron microscopy (EM), as it allows a direct read-out of the size and structural properties. Images in EM are created from accelerated electrons, that after being transmitted or scattered by a sample, hit an electron detector, which due to the short wavelengths of electrons enables sub nm resolution[59]. Since EM experiments are conventionally performed in high vacuum, and since liposomes, virus particles and other BNPs do not withstand dehydration, metal staining and fixation techniques are often required, which in turn changes the size and morphology of the sample [60]. This limitation can be overcome by using cryo-electron microscopy (cryoEM), which makes use of neither staining nor fixation protocols. Instead, a thin film of the NP suspension is spread on a EM support grid and thereafter submerged into liquid nitrogen, which rapidly freezes the water into amorphous ice without forming ice crystals[61]. This process both preserves the material in a native-like state and protects the sample from radiation damage. CryoEM has been employed successfully to characterize individual viruses [60] vesicles [62] and EVs [63–65] to gain insight on both their structural properties and size. In addition to direct structural information, labelling of EVs with antibody-modified gold nanoparticles has been employed to identify sub-populations in the EV preparation [64]. However, the low throughput, complicated sample preparation protocols, long measurement times, and high cost are all limiting factors to make cryoEM a standard BNP analysis tool [66]. A major limitation is high variance due to low sample size, especially for heterogeneous EV samples, as only a limited number of images can be taken in a reasonable amount of time [65]. For example, different properties of nanoscale objects can be extracted by probing them with light. One such method is flow cytometry (FCM), which is used routinely to analyze single cells and smaller particles in the sub-micrometer range [67]. Most flow cytometers work in both scattering and fluorescence mode which combined with immunolabeling allows the structure to be correlated with biomolecular composition [68], although information on size requires that the dependence of the scattering signal on refractive

index and size is known. In FCM, cells or particles in a hydrodynamically-focused fluid stream are illuminated by a laser. Ideally, each cell or particle passes a laser beam one at a time, from where the scattering and fluorescence signals are measured. Since the measured optical signal is dependent on both the size of the particle and its refractive index, this poses one additional limitation, namely that smaller particles will not scatter sufficiently to be detectable during their transit through the illumination volume [69]. This is evident from the fact that the majority of conventional cytometers only detect individual polystyrene beads with a size larger than ~300nm [59,65], while sub-200 nm BNPs, such as viruses and exosomes, remain at the detection limit of conventional flow cytometers due to their weak scattering and fluorescence signals [70].

In response to this shortcoming other methods have been developed, such as dynamic light scattering (DLS) [71], where the size distributions of NP ranging between a few nanometers to several microns can be determined [59], with an impressive limit of detection of down to about 1 nm [72]. In DLS, a dilute suspension containing monodisperse NPs undergoing Brownian motion is illuminated with a focused laser beam [73]. The illuminated NPs scatter light in all directions, which due to their Brownian motion within the illuminated volume leads to temporal fluctuations that depend on particle size. Owing to its broad range of detectable sizes, DLS is used routinely as a high-throughput and sensitive method for accurate size determination [69]. However, for BNP which possess high molecular and dimensional heterogeneity, such as EVs, it remains difficult to accurately determine their size, which is basically because the intensity fluctuations become predominantly influenced by the presence of larger particles [59]. Due to the high heterogeneity and nano-scale size of BNPs, it is important to study these particles on the individual level.

Nanoparticle tracking analysis (NTA) is today one of the most commonly used optical methods for nanoparticle size determination, especially for BNPs such as extracellular vesicles [67] and viruses [74], reaching down to the 50 nm size regime [75]. The underlying principle behind NTA is similar to that of DLS, where particles undergoing random motion in a suspension are illuminated by a focused laser beam. The scattered (or fluorescent) light induced by the particles is then temporally imaged using an objective fitted to a conventional optical microscope, being placed above the sample [76]. However, in contrast to DLS, the imaging mode of NTA makes it possible to analyze the nanoparticles individually, allowing their size to be extracted from their 3-dimensional movement. Unlike DLS, NTA copes better with polydisperse samples, however the quantitative determination of scattering and fluorescent

intensities remain difficult to quantify, since the particles are free to diffuse in and out of the focal plane [70]. NTA was in this work used routinely for BNP size determination, and is discussed in further detail in the Methods section.

Since FCM, DLS nor NTA are best suited to determine scattering / fluorescence intensity or size and do not offer a possibility to unambiguously quantify multiple properties on the level of single nanoparticles, there exists a need for analytical concepts that enable multi-parametric analysis of BNPs. One such method is two-dimensional flow nanometry (2DFN) [10], which offers a detection limit in the sub-30 nm range while simultaneously offering the possibility quantify the scattering / fluorescence intensity by confining them close to a liquid-solid interface in a microfluidic setup. This method was further developed and used in Paper II to quantify the efficiency by which BNPs can be labeled with membrane-specific dyes, and will be therefore discussed more thoroughly in the Experimental Methods section.

Table 1 Comparison of the bioanalytical methods discussed in this chapter

Method	Limit of Detection	Principle	Mode of measurement	Comments
CryoEM	<1 nm	electron transmission	direct, individual	arduous sample preparation, low statistics
FCM	200 nm	light scattering	indirect, individual	multi-parametric
DLS	1 nm	diffusion	indirect, ensemble	monodisperse samples, relative size
NTA	50 nm	diffusion	indirect, individual	polydisperse samples

3 Experimental Methods

3.1 Total Internal Reflection Fluorescence Microscopy

Biological nanoparticles, such as lipid vesicles and other similarly sized objects, cannot be visualized directly with conventional optical microscopy, due to the Abbe diffraction limit as the Airy peaks which arise from each molecule are not separated. Consequently, fluorescent microscopy has been a widely-used method to by-pass the aforementioned issue to visualize and study these nanometer-scale entities. Fluorescent microscopy employs fluorescent molecules, *i.e.* fluorophores¹, for imaging. Importantly, fluorophores can be readily conjugated to molecules such as antibodies and lipids, allowing them to be visualized. A fluorophore is a molecule which has an energy gap usually in the visible range. When a fluorophore absorbs an incoming photon with an energy corresponding to the gap, an orbital electron is brought from the ground state S₀ to the first excited singlet state S₁. This excited state is unstable with a short lifetime, typically in the range of 10⁻⁷ to 10⁻⁹ s. In order to lower its energy, the electron will relax down to the ground state either radiatively or non-radiatively, each with a certain probability. The radiative process from S₁-S₀ with the re-emission of a photon is called fluorescence (Figure 3b) [77]. The re-emitted photon has a longer wavelength (lower energy) than the absorbed, since a small portion of the absorbed energy is converted into vibrational energy, *i.e.* dissipated as heat. All of this is best illustrated on a Jablonski diagram (Figure 3a) [78]. This shift between the excitation wavelength and the emission wavelength of the fluorophore can be utilized for imaging purposes, which was a breakthrough in 1911 [79].

Many different kinds of fluorescence microscopy exist, including confocal laser scanning microscopy [80,81], stimulated emission depletion microscopy [82], and total internal reflection fluorescence microscopy [83], which was the main tool used in this research. Total internal reflection fluorescence (TIRF) microscopy is an extension of conventional fluorescence microscopy, specialized to illuminate only a thin layer on a substrate surface. This technique has been a multifaceted/widely used tool since its invention by Axelrod et al during the 1980s [84] and is based on light travelling between two media with different optical densities (n) in the total internal reflection regime. When a beam of light travels from an optically denser medium and hits the sample interface at an incident angle $\theta_{incident}$ larger than

¹ For a molecule to fluoresce, certain conditions have to be met, such as high rigidity of the molecule, the presence of electron-donor species, and naturally the molecule has to absorb the excitatory light and favor radiative transitions.

the critical angle $\Theta_{critical}$, all light is reflected at the interface. This mechanism is governed by Snell's law, in the case where the angle of refraction becomes 90° :

$$\Theta_{incident} > \Theta_{critical} = \arcsin\left(\frac{n_{low}}{n_{high}}\right), \quad 3.1.1$$

where n_{low} and n_{high} denote the lower and higher optical density materials respectively. However, a non-radiative electromagnetic field confined at the interface called the evanescent field still slightly penetrates a few hundred nanometers into the medium of lower refractive index and decays exponentially with distance from the surface. As the light is totally reflected for angles $\Theta_{incident} > \Theta_{critical}$, then the penetration depth of the evanescent wave can be adjusted by a few hundred nanometers [85]. Using this evanescent wave to excite fluorophores near the surface enables high contrast as the background signal of fluorophores from the bulk is significantly reduced.

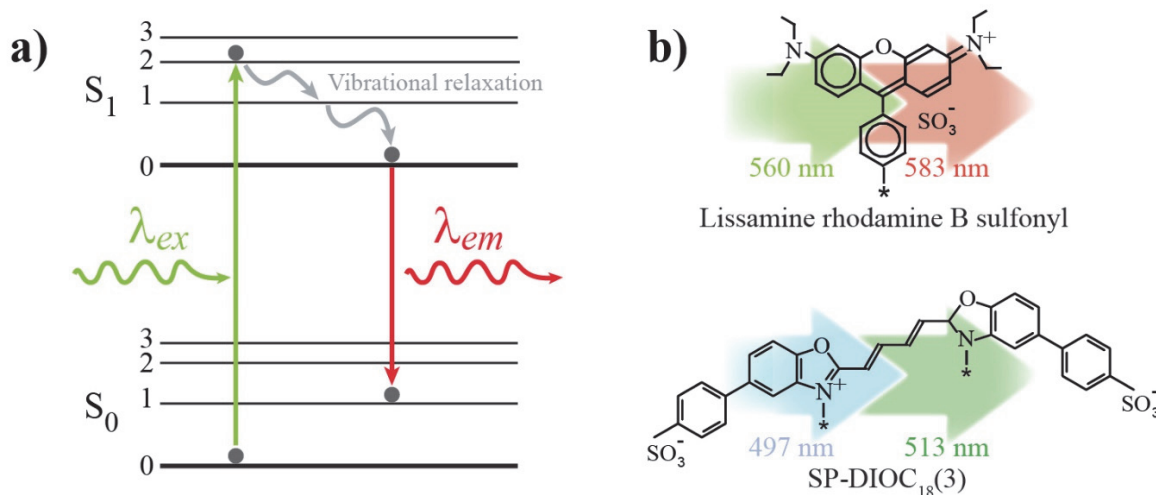


Figure 3. (a) A Jablonski diagram illustrating the concept of fluorescence on an energy plot. (b) Examples of two fluorophores used as lipid conjugated markers in this research – Rhodamine-PE and spDIO (only the fluorescing subunit is shown for clarity). Each fluorophore is overlaid with their typical excitation (left) and emission (right) wavelengths.

In this thesis work, an inverted TIRF microscope was used to image the sample from below, through a transparent borosilicate glass substrate (as shown on Figure 4). Lipid vesicles and SLBs were imaged with this TIRF setup by incorporating two different types of fluorescently-labelled molecules. The vesicles used in the experiments to form SLBs incorporate a fraction of fluorophore-conjugated lipids (Rhodamine-PE), labeled at the hydrophilic head-group of the lipid. However, these lipid-dyes cannot be used with native

membranes without disturbing the membrane environment, as they need to be mixed in via sonication or similar. Therefore, of particular interest is how lipophilic membrane-staining dyes, such as DiO and DiI, which have been utilized routinely to label cell membranes without negatively affecting membrane fluidity [86,87], incorporate into complex BNPs, and how this incorporation depends on particle size, type and molecular composition. Consequently, in the work planned to be summed up in Papers II, SUVs, NMVs and iHSV1 were labelled with the lipophilic membrane-staining dye SP-DiOC₁₈(3)² (hereafter spDIO) which is weakly fluorescent in water but highly fluorescent and quite photostable when incorporated into a lipid membrane.

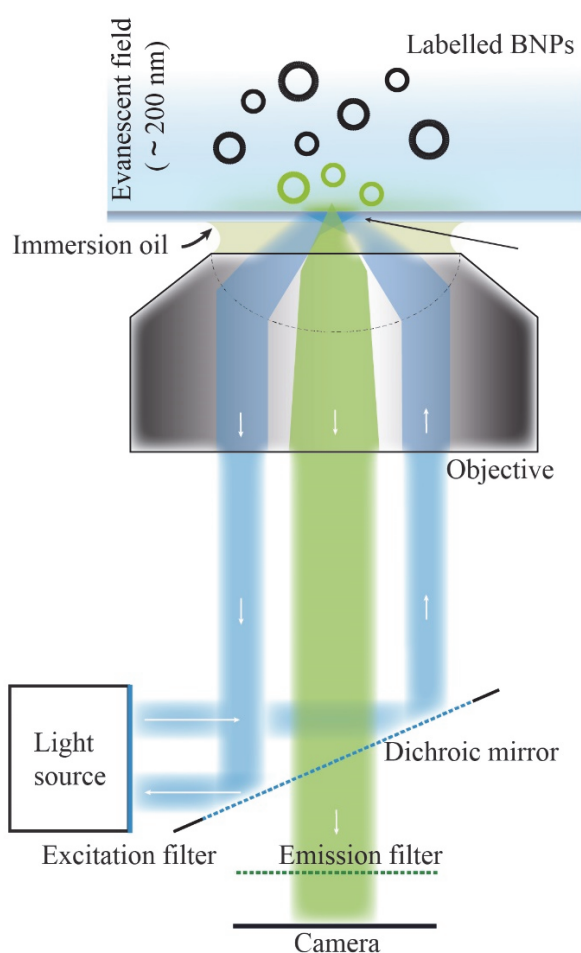


Figure 4. Working principle of TIRF microscopy, highlighting the main components. An off-axis light source is used to impact the sample at a large enough angle to fulfill the total internal reflection condition, resulting in the generation of an evanescent wave, exciting the fluorophores near the surface. A filter cube consisting of an excitation filter, dichroic mirror and an emission filter is present to select and direct the appropriate wavelengths for the fluorophore used, to isolate and image the fluorophore emission from the excitation source.

² 3,3'-Dioctadecyl-5,5'-Di(4-Sulfophenyl)Oxcarbocyanine

3.2 Microfluidics

Microfluidics, as the name states, is the manipulation of fluids in channels with dimensions in the range of micrometers (1-100 μm). In doing so, capabilities that are afforded through the use of microfluidics which bulk chemistry cannot provide include, but are not limited to: (i) the ability to handle very small volumes of liquids (10^{-9} to 10^{-18} liters) and thus, reduce the consumption of samples, solvents and reagents, (ii) laminar flow (characterized by low Reynolds numbers), (iii) high resolution and sensitivity in separation and detection, and (iv) finely controlled flow rates. These unique characteristics can be utilized to promote hydrodynamic shear flow that induces movement of molecules attached to a SLB [88], as discussed in Paper II.

A simple straight microfluidic channel was fabricated from the optically transparent soft elastomer poly-(dimethylsiloxane) (PDMS) using soft-lithography, which is a simple fabrication method based on a molded PDMS stamp [89]. This channel was used in Paper II to enable controlled fluid flows, whereas punched PDMS wells were used in Paper I.

3.3 Size Determination

A multitude of crucial interactions and functions of biological nanoparticles are based on their size. As a result, there is a need to develop sensitive and powerful particle size determination characterization techniques that are capable of detecting sub-200 nm particles and vesicles. Current state-of-the-art particle sizing technologies take advantage of the thermal motion of particles, known as Brownian motion. This random movement of particles was first identified by Robert Brown when he observed small particles ejected from pollen grains undergoing continuous, random motion when dispersed in water. This movement is characterized by rapidly changing velocities due to random collision between solvent molecules, which are in constant thermal motion with a thermal energy in the order of $k_B T$. Collisions between dispersed NPs and solvent molecules occur in all directions and at all interfaces in a motion known as a *random walk*, first characterized by Albert Einstein in 1905 [90]. Einstein determined that the Brownian motion of particles relate to their diffusivity, D , through their mean squared displacement (MSD), which is the measure of particle deviation from its reference position as a function of time [90–92]:

$$MSD(t) = \langle (\mathbf{r}(t) - \mathbf{r}_0)^2 \rangle = 2dDt, \quad 3.3.2$$

where d is the number of dimensions (2 in our case), \mathbf{r}_0 is the reference position of the particle and $\mathbf{r}(t)$ the position at time t . It is important to note that the MSD scales linearly with the

diffusivity, hence allowing one to extract the diffusivity from a linear fit of the curve. The probability distribution of such a particle's displacement follows a Gaussian shape [90].

Most commonly the MSD of an individual particle can be estimated from its experimentally measured trajectory for a given duration $n\Delta t$ (lag time) as follows [91,93,94]:

$$MSD(n\Delta t) = \frac{1}{N-n} \sum_{i=1}^{N-n} (\mathbf{r}_i - \mathbf{r}_{i+n})^2, \quad n = 1, \dots, N-1, \quad 3.3.3$$

where N is the number of frames, \mathbf{r}_i the particle position at frame i , whereas \mathbf{r}_{i+n} the particle position after n frames and Δt the time interval characterized by the frame rate $1/\Delta t$.

Einstein also showed, among others [95,96], how the aforementioned diffusivity relates to the mobility of a particle [90], which is known as the Einstein relation:

$$D = \mu k_B T, \quad 3.3.4$$

The mobility, μ , of a particle is the ratio between an applied drag force F inducing a drift velocity v ($\mu = v/F$) and is inversely proportional to the friction (drag) coefficient, which characterizes the influence of the surrounding medium. In the case of spherical particles at low Reynolds numbers [97], Stokes's law [98] states that the drag coefficient is proportional to the (dynamic) viscosity of the medium and the hydrodynamic radius of the particle. Thus, the Stokes-Einstein equation can be written:

$$D = \frac{k_B T}{6\pi\eta r}, \quad 3.3.5$$

which shows that the diffusivity of a spherical particle depends (except for the thermal energy $k_B T$), only on the viscosity of the solution and the hydrodynamic radius of the particle itself [90].

The aforementioned relation between the size and diffusivity of a particle (eq. 3.3.5) and the possibility to determine the diffusivity from the MSD of a particle's trajectory (eq. 3.3.2) are fundamental for the subsequent methods, as they enable to determine the hydrodynamic size of NPs from their trajectories.

3.3.1 Nanoparticle Tracking Analysis

Nanoparticle tracking analysis (NTA) is one of the most commonly used optical methods for nanoparticle size determination, especially for BNPs such as extracellular vesicles [67]. Conventional NTA uses a focused laser beam to illuminate particles in a suspension. The

particles within the beam scatter light in every direction. This scattered light by each particle in the field of view can then be collected by an objective placed above the sample, fitted to an otherwise conventional optical microscope [76]. The scattered light is captured by a high-speed camera, where the particles ongoing random walks in three dimensions will be visualized as bright/illuminated spots in the field of view. This facilitates individual identification and analysis of single particles by firstly calculating the diffusivity from its two-dimensional MSD (eq. 3.3.2). From this, the hydrodynamic radius of each particle is extracted using the Stokes-Einstein equation (eq. 3.3.5):

$$D = \frac{k_B T}{6\pi\eta r} \xrightarrow{\text{yields}} r = \frac{k_B T}{6\pi\eta D} \quad 3.3.6$$

From this, it is evident that particle diffusivity is inversely proportional to the size of the particles; hence, smaller particles diffuse faster and the diffusivity increases as a function of increasing temperature and decreasing viscosity.

Since conventional NTA operates in scattering mode, with few operating in both fluorescence and scattering mode [69], this size determination method is therefore highly dependent on the refractive index of the particle [99]. Subsequently, for high refractive index materials such as gold, the smallest detectable size is $\sim 30\text{nm}$, whereas the typical size detectable for low refractive index materials, such as lipid vesicles, typically ranges from 70 nm to $1\mu\text{m}$ [59,70] with some examples of size determination down to 50 nm [75]. The upper size limit is due to the inherently slow diffusion of particles larger than $\sim 1\mu\text{m}$, which renders accurate size determination challenging.

Furthermore, there are additional limitations associated with detecting and quantifying particle size distributions using NTA. The trajectory of particles within solution can only be observed as a two-dimensional projection. However, particles are free to move within solution in three-dimensions which causes particles to move in and out of the focal plane. This 3D movement of particles leads to significant errors in the position determination since off-focus particles scatter less than when they are confined within the focal plane. Such particles appear faint or are lost from the field of view altogether. The latter is even more dramatic for smaller NPs, which diffuse faster and have a lower intensity due to a smaller scattering cross-section. Furthermore, particles that are moving in and out of the focal plane, may be re-counted by the algorithm, thus leading to skewed size distributions towards smaller particles.

In principle, NTA can be utilized to estimate the size of a NP based on the fluorescence or scattering intensity. However, this is dependent on the NP remaining within the focal plane throughout the measurement. Since particles are not confined within two dimensions and therefore move in and out of focus, it is rendered difficult to accurately measure their intensity. The 3D movement of particles leads to significant variance in the intensity signals, thus creating unwanted artefacts when attempting to correlate intensity with NP size [100].

3.3.2 2D Flow Nanometry

The limitations associated with conventional NTA can be overcome by confining and restricting the movement of NPs within two dimensions. This was achieved recently by our group by coupling NPs to a fluidic interface, such as an SLB, and thereby enabling the particles to remain within the focal plane for longer residence times [10]. This technique, known as two-dimensional flow nanometry (2DFN), improves the accuracy of intensity and diffusivity estimations substantially, compared to NTA, allowing for precise size determinations of NPs 20-400 nm in diameter.

In order to couple NPs to a fluidic interface, a linker, such as DNA, must be inserted within the membrane of lipid NPs to allow for tethering to a SLB containing mobile complementary DNA. Due to this tethering approach, the theoretical principles used in NTA cannot be applied directly for 2DFN, as the lateral diffusivity of the linker-NP system is controlled mainly by the linker molecule [35], which is significantly slower than a freely moving NP in solution. Specifically, the mobility of tethered particles is defined by the number of NP anchors that are coupled to the fluid interface. In 2DFN, this limitation is overcome by studying the motion of fluorescently-labelled BNPs tethered to a SLB when subjected to a shear flow using a microfluidic channel. In brief, by introducing hydrodynamic shear flow parallel to the SLB, the in-plane movements of BNPs can be monitored using total internal reflection (TIRF) microscopy. In doing so, the individual size of the SLB-tethered BNPs can be elucidated by analyzing their trajectories when subjected to a shear flow [10], the physical principle of which is summarized below.

When a bulk flow of liquid is applied above a planar SLB, the lipid bilayer and its constituents move in the direction of the bulk flow [101] and different sized components move with markedly different velocities. The mobility, μ , of a particle can be deduced from a laminar

bulk flow induced shear force F_{shear} , which creates a directed movement of the particle in the flow direction [90]:

$$\mu = \frac{v_x}{F_{shear}}, \quad 3.3.7$$

where v_x is the flow-directional velocity of the particle. Hence, it can be inferred that a larger force will cause an increase in the particle's velocity. One should also note that the flow directional shear force is equal to the opposing drag force, when the particle is moving at a constant velocity. Furthermore, according to Einstein's relation (eq. 3.3.4), the mobility is also directly related to the diffusivity [90]:

$$\mu = \frac{D}{k_B T}, \quad 3.3.8$$

Thus, the movement of a NP tethered to an SLB under an applied shear force can be divided into two components: (i) directed, non-random NP movement in the flow direction induced by the shear force, and (ii) random movement perpendicular to the flow due to lipids diffusing and interacting with the linker in the membrane. Combining the previous equations 3.3.7 and 3.3.8 yields:

$$\frac{D}{k_B T} = \frac{v_x}{F_{shear}}, \quad 3.3.9$$

By deducing the flow-directional velocity of the NP from the linear increase of the x-position and by measuring the individual trajectories, *i.e.* MSD of tethered NPs in the xy-plane to extract the diffusion coefficient and (Figure 5), the hydrodynamic shear force acting on the NP can be estimated.

Furthermore, the shear force is related to the hydrodynamic radius r of a small spherical particle moving in a viscous fluid under laminar flow via Stokes's law [98]:

$$F_{shear} = 6\pi\eta v_x r, \quad 3.3.10$$

where η is the dynamic viscosity of the surrounding medium, v_x the average velocity of the particle and F_{shear} the shear force acting on the particle.

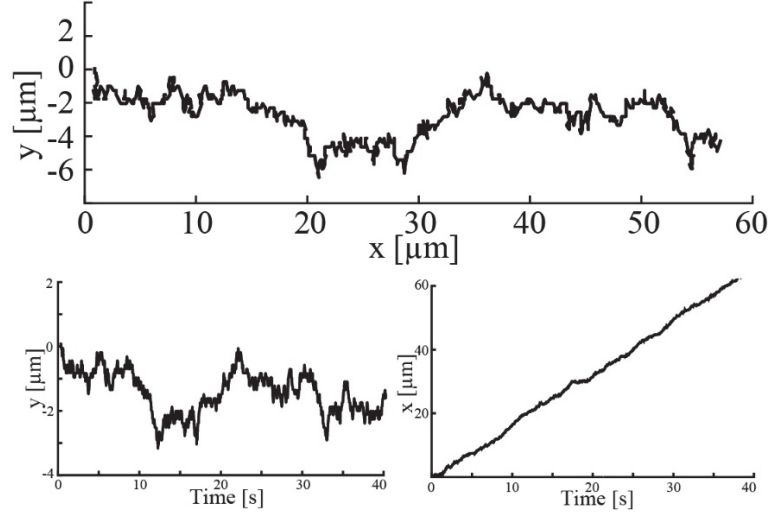


Figure 5. Characteristic track of a tethered BNP, showing the x-directional motion being dominated by a directed movement while the y-directional motion follows random Brownian motion.

Although this equation is valid for a simple (non-tethered) system, some assumptions still need to be made to determine the size distribution of NPs tethered to an SLB. Firstly, the channel height is much larger than the hydrodynamic size of the particle, resulting in a lower flow velocity close to the surface. This is due to the fact, that bulk flow velocity will be larger in the center of the channel than at the walls, floor or ceiling [102]. For laminar flows, the fluid motion is assumed to be a uniform linear shear flow [103–105], hence the macroscopic fluid velocity can be approximated to increase linearly away from the surface (Figure 6a) [101]. Secondly, it is usually assumed that the flow velocity of a viscous fluid close to a surface must be zero, as mass cannot penetrate the solid surface and the cohesive forces between the molecules of the fluid are overcome by their adhesion to the surface [102]. However, there are several reports claiming that this so-called “no-slip” boundary condition is not strictly valid in all scenarios [106–109], thus a slip length must be introduced. The slip length λ can be described as an imaginary distance below the surface where the no-slip boundary condition would otherwise be satisfied (Figure 6a) [109] and can also include the length of the linker molecule. Taking these two assumptions into account, the flow-directional velocity v_x at the center of the tethered NP can be presented as:

$$v_x = v_0(r + \lambda), \quad 3.3.11$$

where v_0 is the laminar flow velocity away from the surface and r the hydrodynamic radius of the NP. Consequently, by combining equations 3.3.10 and 3.3.11, the shear force F_{shear} acting on a particle in a 2DFN experiment can be determined via:

$$F_{shear} = A\eta v_0 r(r + \lambda) \quad 3.3.12$$

where A is a constant that accounts for the channel geometry and possible inhomogeneous flow profile around the NP. It should be noted that neither A nor λ depend on the shape or size of the NP and can be determined via calibration with NPs of known size for a specific channel geometry.

Thus, by measuring the individual trajectories of BNPs, the flow-directional velocity of a nanoparticle (v_x) and the average diffusivity of the NP-linker system (D) can be found. Consequently, if the latter two are known, the hydrodynamic shear force acting on each tracked NP can be directly determined via eq. 3.3.9. The shear force, along with the determined calibration parameters, can subsequently be used to determine the hydrodynamic size of the bound nanoparticles without directly probing a signal proportional to their size (Figure 6b).

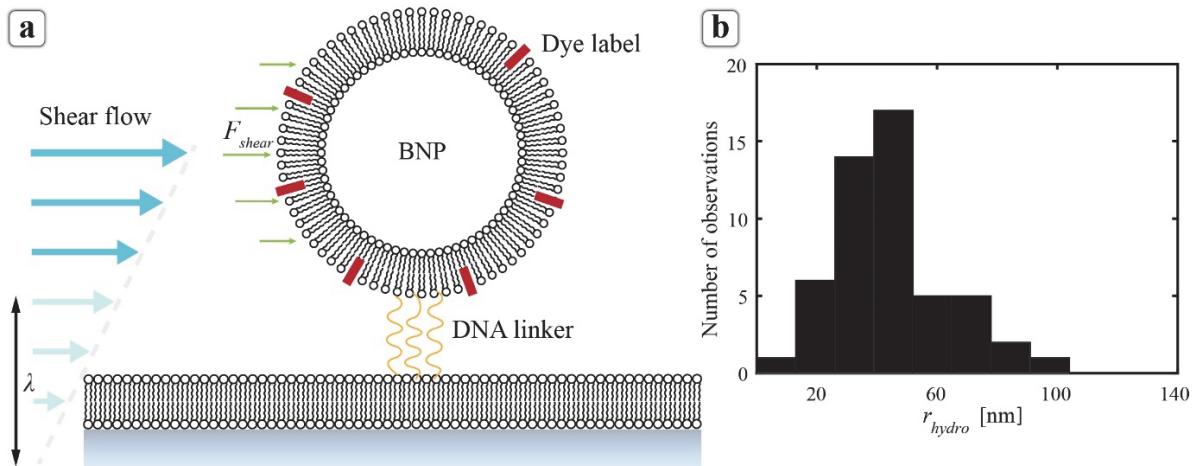


Figure 6. (a) A BNP tethered to a SLB via DNA linkers, experiencing a laminar shear flow, inducing a shear force causing the particle to move in the flow direction. λ indicates the slip length. (b) NMV size distribution acquired with 2DFN.

2DFN offers several key advantages as a size determinant technique, compared to conventional NTA. One clear advantage of 2DFN is the ability to accurately quantify the fluorescence intensity of BNPs. This is done by confining BNPs onto a surface in a TIRF microscopy setup, which allows the probing of only those fluorescently labeled BNPs that are coupled close to the surface. Furthermore, for BNPs with a homogenous surface dye concentration such as vesicles containing lipid-conjugated dyes, the TIRF intensity is expected to be proportional to their size [110]. Therefore, it is possible to correlate the fluorescence intensity of BNPs to their independently determined size. Despite this, it is speculated that dye distribution is commonly inhomogeneous in more complex biological systems, such as viruses

and exosomes, where lipid-conjugated dyes cannot be used. Thus in Paper II, it was the intention to use the aforementioned technique combined with TIRF microscopy to determine the size, independent of fluorescent intensity, of the following BNP systems: artificial lipid vesicles, NMVs and enveloped herpes simplex virus type 1 (HSV1). Due to problems to tether NMVs and HSV1 to the membrane, results for these systems remains to be included.

3.3.2.1 Data analysis

The data analysis of 2DFN is very sensitive to several parameters, which will be discussed more thoroughly below.

One such parameter is distance cutoff, determining whether it is a unique particle that is followed, *i.e.* if it belongs to a unique track, which is defined by a maximum distance between two ‘particles’ in two consecutive frames. This value is dependent on the surface coverage of the particles, since in order to avoid linking of two different particles in close proximity it must be lowered when the density is high. This value is selected by using a large distance cutoff and plotting all mean squared displacements. By linearly fitting the initial data points, it is possible to evaluate where the true tracks meet the noise (the false linking events). This intersection (Figure 7) then defines the cutoff value that is used in the analysis.

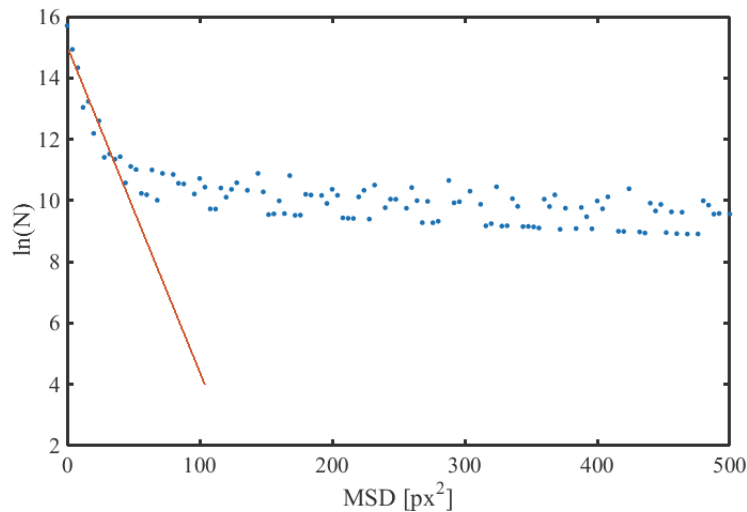


Figure 7. Logarithmic representation of the normalized count as a function of MSD. The cutoff value is evaluated at the intersection where the linear fit (red line) crosses the average noise, which in this case is 50.

For accurate intensity determination, several parameters which help mitigating the influence of potential bleaching and other factors have to be chosen very carefully, since the resulting intensity distribution can be affected by several factors, such as uneven illumination, tracking errors, dye transfer to the SLB and mode of illumination (TIRF vs. EPI). Due to the aforementioned factors, the intensity of an individual particle can fluctuate quite significantly along the particle trajectory as it moves across the field-of-view. Typically, the average intensity throughout the whole trajectory is measured, but this would result in unnecessary fluctuations. Therefore, to lower the fluctuations, the intensity was determined in the middle 100px of the field-of-view, where the TIR light hits the sample and consequently results in the highest signal-to-noise. Furthermore, to remove any potential tracking errors, which cannot be excluded with the distance cutoff, *e.g.* the linkage of two particles which are in close proximity, tracks with unreasonably large fluctuations around their average intensity value were removed. This was done by first measuring the intensity over time for a few immobile particles per movie. The particle with the highest standard deviation relative to its mean value was used as an upper limit, to include everything below that value in the intensity versus size graph. Specifically, this relative standard deviation of the intensity ranged between 10-25%. Last, only particles which were present in the beginning 1/3 of the field-of-view, were included in the analysis to exclude particles which are lost during tracking and may later be found again, thus resulting in double-counting. However, this condition will often only marginally affect the result, as the other conditions are sufficient to remove any tracking errors.

4 Results

The findings addressed in this thesis are captured in two papers, which are summarized and detailed below.

4.1 Paper I

Supported lipid bilayers (SLBs) mimic several key features of cellular membranes, such as planar geometry and fluidic freedom. In all studies concerning SLBs, the quality of the SLB is a critical factor that influences its function and utility. Therefore, significant efforts have been invested to gain an in-depth understanding of the SLB formation process [26,27,111–116]. Further, utilizing SLB's as a core of our measurement approach (Paper II), places specific weight upon highly reproducible SLBs. Therefore, in Paper I, we employed TIRF microscopy to study the SLB formation process and kinetics on borosilicate glass. In comparison to how fluorescence microscopy was previously employed to study SLB formation [117,118], we labelled only a small fraction (1%) of the vesicles, allowing the individual adsorbed vesicles and SLB patches to be monitored simultaneously, by simultaneously increasing the optical contrast between SLB patches and their surrounding regions [56]. Resolving individual vesicles allowed the entire SLB formation process to be observed, from individual vesicles to small SLB patches, and finally coalescence to a full SLB. To quantify the individual SLB patch evolution and variances in patch-growth scenarios, the boundary of each patch was measured for each analyzed time point and subsequently used to calculate the average front velocity. It was concluded from our analysis that the average front velocity increases dramatically, up to one order of magnitude, despite the fact that the surface density of adsorbed vesicles increases only marginally by about 8% (Figure 8). This finding is considered significant as typically the front velocity of a spreading lipid mono-or bi-layer front on hydrophobic and hydrophilic surfaces, respectively, is either decreasing or stagnant over time [119–121].

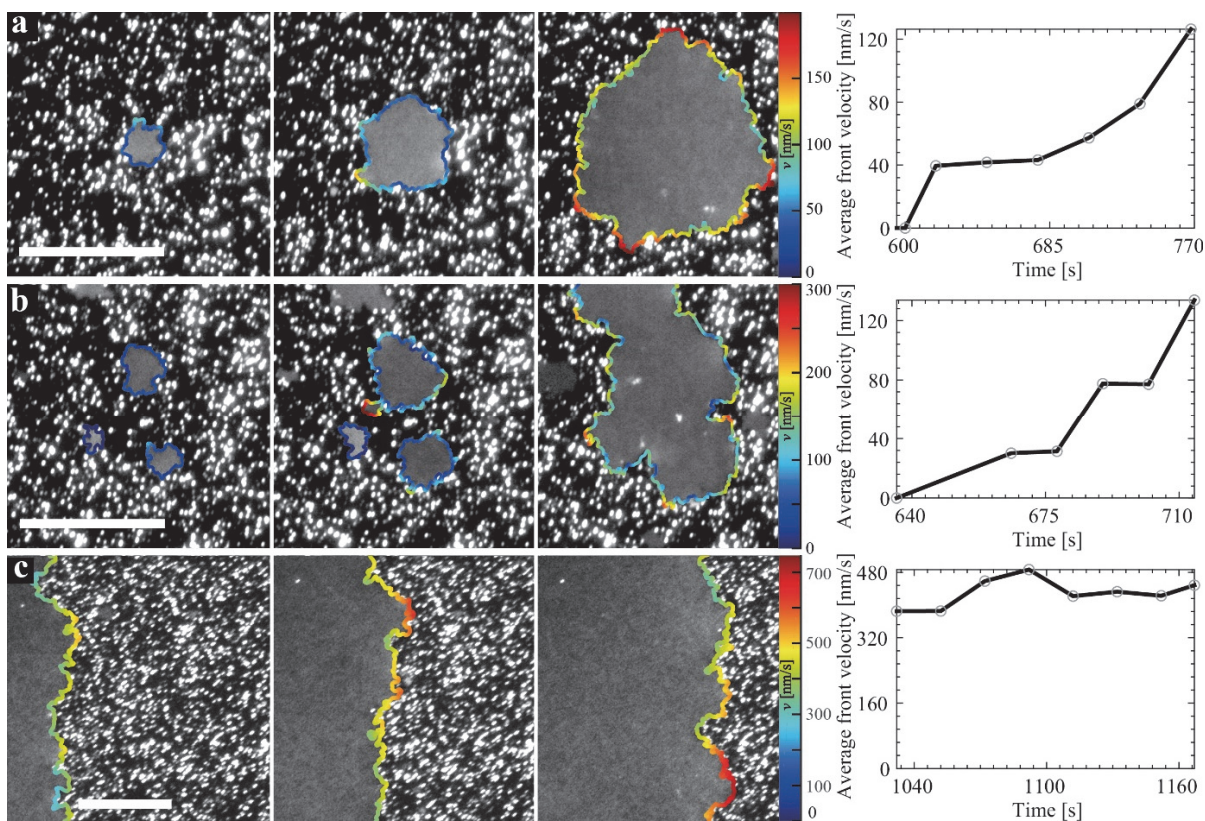


Figure 8. Typical patterns observed during the SLB patch growth and the corresponding dependence of the average front velocity with time: (a) single patch formation and expansion (snapshot interval 60 s), (b) small patches merging into a bigger patch (snapshot interval 24 sec), and (c) propagating SLB front (snapshot interval 30 sec). Scale bars represent 20 μm . The color of the perimeter lines used in the images, indicates the local front velocity of the SLB patch.

To theoretically address the rate of SLB growth, two different scenarios regarding the incorporation of lipids into the SLB patch after the rupture were examined: *local relaxation* and *global relaxation*. In the *local relaxation* scenario, the lipids belonging to a ruptured vesicle are assumed to form a circular SLB, where the growth is restricted to the immediate vicinity of each ruptured vesicle. In this scheme, no significant lipid rearrangement in newly-formed patches occurs, implying that the overlap with the existing SLB patches can be interpreted as either a double bilayer or material loss. In the *global relaxation* scenario, all lipids from ruptured vesicles will instead rapidly diffuse along the substrate and merge with the patch inducing their rupture, resulting in a circular SLB. The majority of the experimental observations followed the *global relaxation* model, manifesting in increasing front velocities (Figure 8). The global model also describes the observed cases, where the local coverage of vesicles was low. In these cases, the growth halted until more material for sustainable growth was introduced.

4.2 Paper II

The development and advancement of novel nanoparticle size determination and characterization techniques is integral for improved understanding of cellular processes involving biological nanoparticles (BNPs), such as cellular communication and viral infections [2,50,53,122]. Since BNPs are usually highly heterogeneous in nature, there is a demand for techniques that provide simultaneous information of multiple parameters, such as size and concentration, preferably with single BNP resolution. In an attempt to achieve this, TIRF microscopy was combined with microfluidics, in Paper II, to study a BNP model system consisting of fluorescently-labelled liposomes tethered to a supported lipid bilayer (SLB). Two-dimensional flow nanometry (2DFN) was utilized in this approach by applying shear force to the liposomes, allowing for the Brownian motion of tethered liposomes to be decoupled from their directed motion. In doing so, the hydrodynamic size and fluorescent emission could be determined independently for each tracked liposome [10].

In previous work, it was verified that fluorescence intensity could be correlated to liposome size for a fluorescent lipid-dye (Rh-POPE), which was incorporated during vesicle fabrication/generation [10]. However, dye-labeled lipids cannot be incorporated into native membranes without severely disturbing the lipid organization, since they need to be combined by lysing the membrane through sonication or similar. Subsequently, the objective of Paper II was to utilize 2DFN to independently derive the size and fluorescence intensity of model BNPs with varying complexities, ranging from artificial liposomes to viruses, using the lipophilic-staining dyes, spDIO and PKH, which have been routinely utilized to label cell membranes without negatively affecting membrane fluidity [86,87]. Despite the extensive use of lipophilic dyes, it still remains unclear how they are incorporated into complex BNPs, and how this incorporation depends on particle size, type and molecular composition. Subsequently, specific emphasis was placed on investigating the correlation between the dye incorporation efficiency and BNP size.

To address this, a model system consisting of liposomes containing either lipophilic dye, spDIO or PKH, was used to measure the incorporation efficiency of the dye in the liposome. This was achieved by quantifying and relating the fluorescence intensity emitted by the liposomes to their sizes on an individual level. For all of dyes used, the fluorescent intensity of the liposomes scaled with their surface area, making the approach highly feasible for qualitative determination of incorporation efficiencies of fluorescent dyes. Figure 9 shows how the size

and intensity of spDIO-labelled POPC indeed follows the expected dependency. We also addressed the issue of nonspecific binding on lipid vesicles to the SLB, and discuss the appropriateness of the inclusion of these nanoparticles into the analysis. It can thus be anticipated that other lipophilic dyes, with a similar molecular composition, will behave in a comparable manner. For more complex, real BNPs, labelled with lipophilic dyes, this scaling is however not obvious, as also indicated from results obtained using spDIO and NMVs.

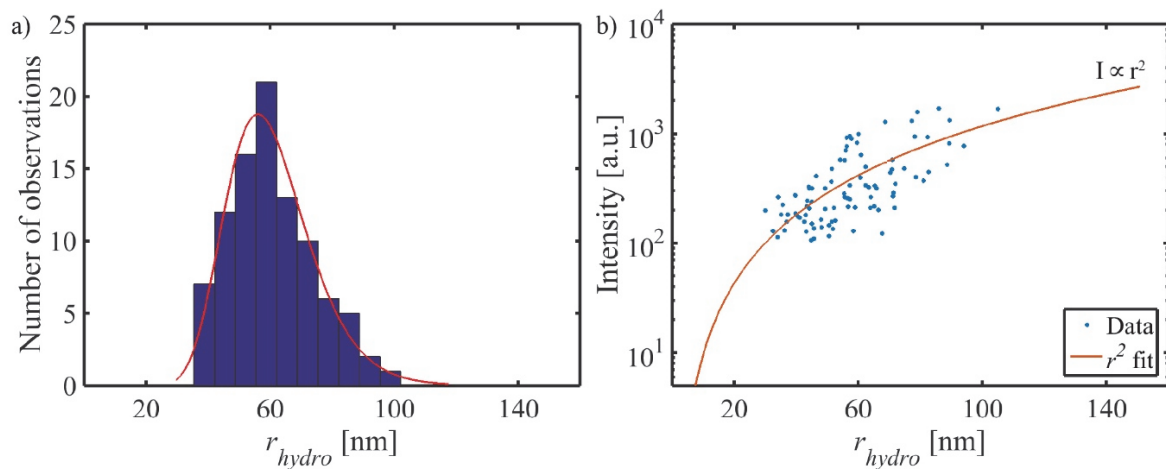


Figure 9. a) Size distribution determined using 2DFN (blue) of spDIO-labelled DNA-tethered vesicles fitted to a log-normal distribution (red). b) Fluorescence intensity versus hydrodynamic radius (blue dots) for spDIO-labelled DNA-tethered liposomes

5 Future outlook

In addition to paper I and II included in the licentiate thesis, there are several other ongoing and prospective projects furthering nanoparticle characterization, which will be discussed below.

5.1 Size and intensity correlation of complex BNPs

Several BNPs were studied in the context of this thesis – Rhodamine, PKH and spDIO labelled POPC vesicles, as well as spDIO labelled NMVs, EVs and iHSV1s. However, the experiments were always not as straightforward as one would hope. Since the 2DFN approach typically requires a tethering chemistry, such as cholesterol DNA, it is necessary to know the concentration of the stock BNP. However, the concentration of complex BNPs samples is typically unknown and can differ from sample-to-sample. Nonetheless, NTA was used in these cases to estimate the number concentration of EVs and iHSV1. Moreover, in a typical 2DFN experiment approximately 3-10 tethers per BNP should be used depending on the size of the particles, to ensure linker-dominated diffusivity while still retaining sufficient mobility [10,123]. To illustrate a common challenge, we aimed at taking these two factors into account when EVs were incubated with cholesterol-DNA to achieve 6, 12, 30, and 60 DNAs per particle. Subsequently, EVs with increasing tether concentrations were introduced to the flow channel containing a complementary cholesterol-DNA incubated SLB. However, no binding was observed in any of these cases, although the particles were clearly visible in bulk. One of the reasons for the absence of binding could be insufficient amount of tethers per particle, since the stock and consequently incubation concentration of EVs determined from NTA compared to POPC was over 50 times lower. If the true EV concentration is significantly higher (NTA does not detect vesicles below a certain size), the concentration of cholesterol-DNA used to modify the EVs might have been too low. This is however quite unlikely, since cholesterol-DNA should have enough time to diffuse and incorporate into EVs within the incubation time and since one cholesterol-DNA per vesicle should be enough to observe at least transient binding. However, the reasoning is based on the reasonable assumption that self-insertion of cholesterol-DNA into phospholipid membranes is efficient in EVs. In fact, self-insertion of amphiphilic compounds like cholesterol-DNA may very well be hindered by the already high membrane cholesterol content of these native BNPs, making them effectively highly rigid particles. In fact, after EVs were incubated with spDIO, a visual red-shift (from yellow to pink) in the color of the sample was observed. The latter could be caused by a high amount (~30%) of cholesterol in the membrane of the EV, also obstructing the subsequent cholesterol-DNA

incorporation into the membrane. In turn, the free cholesterol DNA in the EV solution potentially covered most of the available binding sites on the SLB. Interestingly, the post-labelled EVs were exceptionally bright compared to POPC vesicles, ensuring the applicability of these lipophilic dyes for complex BNP labelling. In future work, we will put focus on alternative tethering schemes, such as cholesterol-modified PEG with a biotin anchor for binding to streptavidin on an SLB or only electrostatic attraction (see Paper II). These issues, which were also observed for HSV1 and NMVs, stimulated the use of the high throughput device described in the next section, in which case there is no need for a tethering chemistry.

5.2 High throughput device

Another ongoing project is the characterization of exosomes and other BNPs in a high-throughput device. Contrarily, with this method, individual particles are confined in high-aspect ratio nanochannels of 300 nm in both width and height, but several millimeters in length. As the particles are of similar size-scale to the channel cross-section, they will be unable to diffuse perpendicularly along the flow and will experience hindered diffusion [124]. However, the size of BNPs can be still estimated from their flow-directional diffusivity by taking the aforementioned corrections into account. Furthermore, as these NPs stay within the focal plane, the intensity determination will be similar to the 2DFN case. This will enable the determination of size and intensity distributions of different BNPs in a high-throughput manner. Figure 10 shows a dataset with Rhodamine-labelled vesicles, depicting a correlation between the size and concentration of these particles. Furthermore, the size distribution in this case does not need adjustment or calibration, as the size of each BNP is calculated directly from their diffusivity according to equation 3.3.6 by taking into account the effect of the walls [124], illustrating the applicability of this method for non-tethered nanometer-scale biological systems

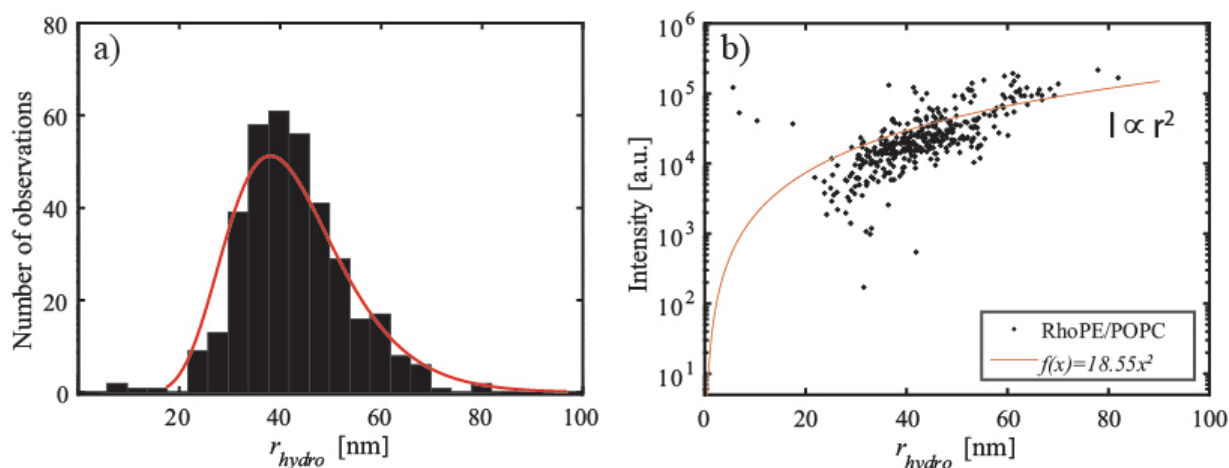


Figure 10. Analysis of Rhodamine-labelled vesicle (a) size distribution with a log-normal fit (line) and (b) intensity versus hydrodynamic radius dependence determined using the hindered diffusion model. The fit demonstrates an r^2 dependence, with an R-square value of 0.45.

5.3 Concentration determination

In addition to size, molecular content and structure, one would also like to acquire information about the concentration of BNPs, since it is believed that the concentration of specific EVs, *e.g.* exosomes, is altered for patients affected with disease compared to healthy subjects [125]. Recently, Rupert *et al.* used surface plasmon resonance spectroscopy to determine exosome concentration in solution from the rate of exosome binding under diffusion limited conditions [126]. We planned to further this research by measuring both the rate binding of individual vesicles to an SLB combined with the 2DFN approach described in section 3.3.2 and Paper II. The adsorption kinetics of vesicles can be investigated by either directly measuring the rate of binding to a surface or to an SLB via tethering-chemistry. The rate of adsorption to the surface can follow two pathways: (i) reaction-limited binding, where the binding kinetics is determined by the actual binding to the surface or (ii) diffusion-limited binding, where the binding to the surface is so fast that the rate of binding is controlled by diffusion across a depletion zone near the surface. For rectangular flow geometry, the mass transfer to the surface can be characterized by the mass-transport coefficient [127,128]:

$$k_M = 0.98 \left(\frac{D_i}{h} \right)^{\frac{2}{3}} \left(\frac{Q}{wl} \right)^{\frac{1}{3}}, \quad 5.3.1$$

where D_i is the diffusion coefficient of the vesicle population with size i , Q the volumetric flow rate, and h , w , l are the height, width, and length of the channel, respectively. The rate of binding is then proportional to the analyte concentration according to [111,129]:

$$\frac{\Gamma_i}{\Delta t} = k_M C_i, \quad 5.3.2$$

where $\Gamma_i/\Delta t$ is the rate of binding per surface area of vesicle subpopulation with size i and C_i is the concentration of the corresponding subpopulation. However, the adsorption rate to the surface under flow conditions may differ at various points on the surface, depending on the distance from the inlet to the measurement area [111]. Therefore, we designed a PDMS chip (Figure 11a) to minimize effects from depletion and buildup of a depletion layer, which can be caused due to liquid passage between the measurement area and the sample container. In order to test the PDMS chip design, we measured several time series of Rhodamine-labelled POPC vesicles binding to the glass floor of a microfluidic chip. Figure 11b shows two binding experiments with the same flow rate, but in different regions of the PDMS chip. The higher rate of binding was observed in the second region of the channel, which consequently lead to differences in the calculated concentrations. The concentration was calculated according to eq. 5.3.2 and compared to the concentration value estimated from the molar concentration of vesicles in the prepared solution. The latter was estimated by using the mode size from NTA to calculate the amount of lipids per vesicle. While comparing these two values an average of 92% (out of >10 experiments) of the prepared concentration was achieved in the second region of the channel. In principle, this result suggested that the chip design was suitable for further experiments. However, 30% of the cases were outliers, being off by a factor of 2. The discrepancy between the prepared concentration and the concentration calculated using eq. 5.3.2 can be attributed to several factors. First, some material may be lost through sample preparation *e.g.* extrusion and subsequent dilution steps. However, a more probable reason to the discrepancy is the assumption of using the mode value from NTA to estimate the prepared vesicle concentration. This could be overcome by taking into account the whole NTA size distribution in the calculation of the initial vesicle concentration from the dry lipid concentration.

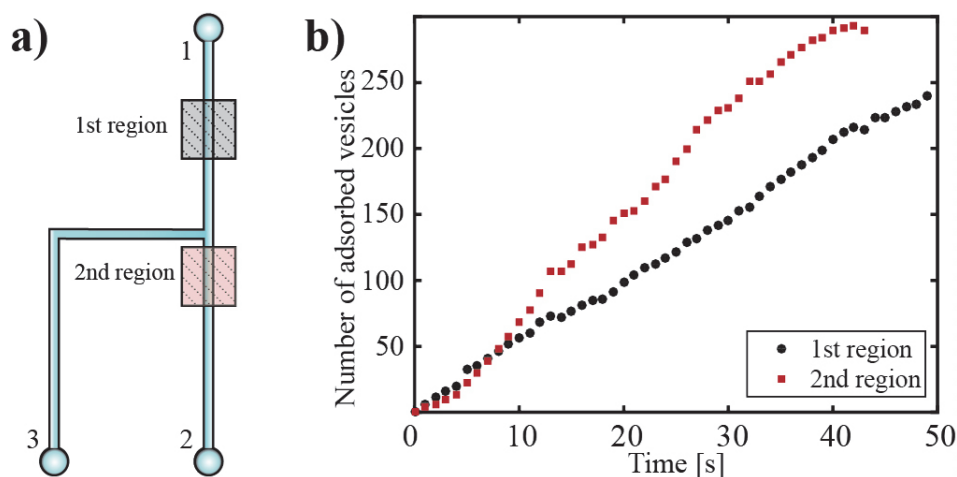


Figure 11. Microfluidic flow chamber specifics (a) Schematic of the channel geometry. Two equal flows of the sample from inlet 1, and buffer from inlet 2, are introduced simultaneously. During this introduction, a fluorescent time series of images is taken in the 1st region. Following this, outlet 3 is closed, and inlet 2 is opened. Another time series is taken in the 2nd region. (b) Number of detected vesicles within the 1st (black dots) and 2nd (red squares) regions of the channel plotted versus time, for a $100 \times 100 \mu\text{m}^2$ surface area.

This approach can in principle be extended to BNP binding to an SLB. However, it remains difficult to combine both the size and concentration determination in one experiment, to in that way determine both the concentration of differently sized particle sub-populations and molecular content. In order to ensure mass-transport limited conditions, a high-affinity binding chemistry such as neutravidin-biotin is needed. However, particles tethered in this way are not easy to shear with a hydrodynamic flow. Another option is to continue with DNA-tethering, with mobile vesicles as was done in 2DFN. This might switch the rate of binding to the reaction-limited regime, but it may increase the possibility of elucidating the concentration by determining the rate for the reaction limited binding process. Alternatively, as the 2DFN method can be used to determine if a specific BNP-dye combination incorporates proportionally to particle size (Paper II), this approach could be combined with the concentration determination of BNPs obtained from the rate by which they bind to the surface. In this way, one could thus determine both the concentration and individual size of complex BNP sub-populations. In either case, this would enable for the method to become truly multi-parametric, by enabling one to determine the size, concentration and molecular content – all in one experiment.

5.4 Native drug-delivery vehicles

Since drug delivery vehicles made of synthetic lipid encounter a multitude of limitations for *in vivo* applications, much interest has been focused on harnessing BNPVs for drug-delivery applications [130]. For example, limitations such as poor uptake and non-specific drug release can potentially be overcome by using NMVs (more thoroughly discussed in section 1.3.3), which are obtained via mechanical cell lysis [56], or exosomes [131]. Compared to synthetic vesicles, NMVs have high biocompatibility, long retention time *in vivo* and efficient cellular uptake [132]. Further, NMVs can be combined with mesoporous silica nanoparticles (MSNs) which have several beneficial properties – tunable size, high stability, high biocompatibility, high drug loading, and controlled drug release [133]. In future work, we will explore this possibility by sonicating NMVs together with MSNs, similarly to how synthetic vesicles were previously used for the same purpose [134]. To validate if the MSNs are lipid coated, both membrane dyes and TEM will be used (having uncoated bare particles as the control) [135]. If protocols can be found to ensure the encapsulation of MSNs was effective, we plan to determine if cellular uptake of native MSNs is increased *in vivo*, compared to non-native protocells.

6 Acknowledgements

First of all I would like to thank my supervisors *Fredrik Höök* and *Gavin Jeffries*, for your wise words and support throughout my PhD journey. *Fredrik*, has always fascinated me with this numerous ideas and visions, whereas *Gavin* is co-supervising me even after leaving academia!

The following people have made a major impact in my professional life, either by giving me valuable advice in the lab (*Quentin, Mokhtar* and *Björn, son of Agnar*) and/or fostering interesting discussions in the fika corner (*Nadia, Karin* and *Nagma*). Regarding the latter, I have not forgotten all the past and current members of the *Biological Physics Group*, who have accelerated these crazy discussions and otherwise made my work (and after-work) life enjoyable. Thank you!

There are also some people, who have left Chalmers during this time whom I dearly miss – *Hudson, Marta, Olov, Nagma*, and now *Nadia* as well.

I thank *Paul* for proof-reading this thesis and otherwise supporting me.

A special shout-out goes to *Kiryl*, my beloved comrade and *Bella* for being always so cheerful.

I would also like to acknowledge all my co-authors that contributed to my publications.

Thank you *Margit* for tolerating my anxiety and all my friends whom I've met in Sweden for supporting me!

Viimaks ei tohiks ju unustada ka oma kallist ema, kes on ju kõige enam minu ärevust ja meeleheidet kuulnud ning neid kalleid sõpru, kellega ma ikka ja jälle üritan Eestisse sattudes kokku saada ja muljetada ☺

Like Gollum said, some things really are 'My precious!'

References

- [1] M. Prince, A. Comas-Herrera, M. Knapp, M. Guerchet, et al., World Alzheimer Report 2016 Improving healthcare for people living with dementia. Coverage, Quality and costs now and in the future, *Alzheimer's Dis. Int.* (2016) 1–140. doi:10.13140/RG.2.2.22580.04483.
- [2] E. Barrow, A. V Nicola, J. Liu, Multiscale perspectives of virus entry via endocytosis, *Virology* 10 (2013) 177. doi:10.1186/1743-422X-10-177.
- [3] G. Raposo, W. Stoorvogel, Extracellular vesicles: Exosomes, microvesicles, and friends, *J. Cell Biol.* 200 (2013) 373–383. doi:10.1083/jcb.201211138.
- [4] C. Quek, A.F. Hill, The role of extracellular vesicles in neurodegenerative diseases, *Biochem. Biophys. Res. Commun.* 483 (2017) 1178–1186. doi:10.1016/j.bbrc.2016.09.090.
- [5] L. Zhu, K. Wang, J. Cui, H. Liu, et al., Label-Free Quantitative Detection of Tumor-Derived Exosomes through Surface Plasmon Resonance Imaging, *Anal. Chem.* 86 (2014) 8857–8864. doi:10.1021/ac5023056.
- [6] K.M. Candelario, D. a Steindler, The role of extracellular vesicles in the progression of neurodegenerative disease and cancer., *Trends Mol. Med.* 20 (2014) 368–74. doi:10.1016/j.molmed.2014.04.003.
- [7] R. Bello-Morales, B. Praena, C. de la Nuez, M.T. Rejas, et al., Role of microvesicles in the spread of Herpes simplex virus type 1 in oligodendrocytic cells, *J. Virol.* 92 (2018) JVI.00088-18. doi:10.1128/JVI.00088-18.
- [8] M. Santiana, S. Ghosh, B.A. Ho, V. Rajasekaran, et al., Vesicle-Cloaked Virus Clusters Are Optimal Units for Inter-organismal Viral Transmission, *Cell Host Microbe.* 24 (2018) 208–220.e8. doi:10.1016/j.chom.2018.07.006.
- [9] B. György, T.G. Szabó, M. Pásztói, Z. Pál, et al., Membrane vesicles, current state-of-the-art: emerging role of extracellular vesicles, *Cell. Mol. Life Sci.* 68 (2011) 2667–2688. doi:10.1007/s00018-011-0689-3.
- [10] S. Block, B.J. Fast, A. Lundgren, V.P. Zhdanov, et al., Two-dimensional flow nanometry of biological nanoparticles for accurate determination of their size and emission intensity, *Nat. Commun.* 7 (2016) 12956. doi:10.1038/ncomms12956.
- [11] S.R. Tabaei, J.J.J. Gillissen, S. Block, F. Höök, et al., Hydrodynamic Propulsion of Liposomes Electrostatically Attracted to a Lipid Membrane Reveals Size-Dependent Conformational Changes, *ACS Nano.* 10 (2016) 8812–8820. doi:10.1021/acsnano.6b04572.
- [12] B. Alberts, A. Johnson, J. Lewis, M. Raff, et al., *MOLECULAR BIOLOGY OF THE CELL, 5TH EDITION*, 2007. <http://www.amazon.com/Molecular-Biology-Cell-Bruce-Alberts/dp/0815341059>.
- [13] R.A.L. Jones, *Soft condensed matter*, Oxford University Press, 2003.
- [14] D.B. Fenske, M.A. Monck, P.R. Cullis, M.J. Hope, The functional roles of lipids in biological membranes, in: *Biomembr. A Multi-Volume Treatise*, 1995: pp. 1–28. doi:10.1016/S1874-5342(06)80053-X.
- [15] E. Fahy, S. Subramaniam, H.A. Brown, C.K. Glass, et al., A comprehensive classification system for lipids, *J. Lipid Res.* 46 (2005) 839–862. doi:10.1194/jlr.E400004-JLR200.
- [16] G. van Meer, D.R. Voelker, G.W. Feigenson, Membrane lipids: where they are and how they behave, *Nat. Rev. Mol. Cell Biol.* 9 (2008) 112–124. doi:10.1038/nrm2330.
- [17] R.B. Gennis, *Biomembranes: molecular structure and function*, Springer New York, New York, NY, 1989. doi:10.1007/978-1-4757-2065-5.
- [18] R. Breslow, Hydrophobic effects on simple organic reactions in water, *Acc. Chem. Res.*

- 24 (1991) 159–164. doi:10.1021/ar00006a001.
- [19] Y.-H.M. Chan, S.G. Boxer, Model membrane systems and their applications., *Curr. Opin. Chem. Biol.* 11 (2007) 581–7. doi:10.1016/j.cbpa.2007.09.020.
- [20] N. Jacob, N. Israelachvili, *Intermolecular and Surface Forces*, Elsevier, 2011. doi:10.1016/C2011-0-05119-0.
- [21] J.N. Israelachvili, S. Marcelja, R.G. Horn, Physical principles of membrane organization., *Q. Rev. Biophys.* 13 (1980) 121–200. doi:10.1017/S0033583500001645.
- [22] L.K. Tamm, H.M. McConnell, Supported phospholipid bilayers., *Biophys. J.* 47 (1985) 105–13. doi:10.1016/S0006-3495(85)83882-0.
- [23] S.J. Johnson, T.M. Bayerl, D.C. McDermott, G.W. Adam, et al., Structure of an adsorbed dimyristoylphosphatidylcholine bilayer measured with specular reflection of neutrons., *Biophys. J.* 59 (1991) 289–94. doi:10.1016/S0006-3495(91)82222-6.
- [24] E.T. Castellana, P.S. Cremer, Solid supported lipid bilayers: From biophysical studies to sensor design, *Surf. Sci. Rep.* 61 (2006) 429–444. doi:10.1016/j.surfrep.2006.06.001.
- [25] H. Schönherr, J.M. Johnson, P. Lenz, C.W. Frank, et al., Vesicle Adsorption and Lipid Bilayer Formation on Glass Studied by Atomic Force Microscopy, *Langmuir.* 20 (2004) 11600–11606. doi:10.1021/la049302v.
- [26] J.M. Johnson, T. Ha, S. Chu, S.G. Boxer, Early steps of supported bilayer formation probed by single vesicle fluorescence assays., *Biophys. J.* 83 (2002) 3371–9. doi:10.1016/S0006-3495(02)75337-X.
- [27] C.A. Keller, K. Glasmästar, V.P. Zhdanov, B. Kasemo, Formation of Supported Membranes from Vesicles, *Phys. Rev. Lett.* 84 (2000) 5443–5446. doi:10.1103/PhysRevLett.84.5443.
- [28] I. Gözen, A. Jesorka, Instrumental Methods to Characterize Molecular Phospholipid Films on Solid Supports, *Anal. Chem.* 84 (2012) 822–838. doi:10.1021/ac203126f.
- [29] J. Salafsky, J.T. Groves, S.G. Boxer, Architecture and Function of Membrane Proteins in Planar Supported Bilayers : A Study with Photosynthetic Reaction Centers †, 2960 (1996) 14773–14781.
- [30] P.S. Cremer, S.G. Boxer, Formation and Spreading of Lipid Bilayers on Planar Glass Supports, *J. Phys. Chem. B.* 103 (1999) 2554–2559. doi:10.1021/jp983996x.
- [31] R.P. Richter, A.R. Brisson, Following the Formation of Supported Lipid Bilayers on Mica: A Study Combining AFM, QCM-D, and Ellipsometry, *Biophys. J.* 88 (2005) 3422–3433. doi:10.1529/biophysj.104.053728.
- [32] R.P. Richter, R. Bérat, A.R. Brisson, Formation of Solid-Supported Lipid Bilayers: An Integrated View, *Langmuir.* 22 (2006) 3497–3505. doi:10.1021/la052687c.
- [33] K. Dimitrievski, B. Kasemo, Simulations of Lipid Vesicle Adsorption for Different Lipid Mixtures, *Langmuir.* 24 (2008) 4077–4091. doi:10.1021/la703021u.
- [34] I. Czolkos, A. Jesorka, O. Orwar, Molecular phospholipid films on solid supports, *Soft Matter.* 7 (2011) 4562. doi:10.1039/c0sm01212b.
- [35] I. Pfeiffer, F. Höök, Bivalent Cholesterol-Based Coupling of Oligonucleotides to Lipid Membrane Assemblies, *J. Am. Chem. Soc.* 126 (2004) 10224–10225. doi:10.1021/ja048514b.
- [36] J.J. Benkoski, F. Höök, Lateral Mobility of Tethered Vesicle–DNA Assemblies, *J. Phys. Chem. B.* 109 (2005) 9773–9779. doi:10.1021/jp044947p.
- [37] K.J. Seu, A.P. Pandey, F. Haque, E.A. Proctor, et al., Effect of Surface Treatment on Diffusion and Domain Formation in Supported Lipid Bilayers, *Biophys. J.* 92 (2007) 2445–2450. doi:10.1529/biophysj.106.099721.
- [38] T. Charitat, E. Bellet-Amalric, G. Fragneto, F. Graner, Adsorbed and free lipid bilayers at the solid-liquid interface, *Eur. Phys. J. B.* 8 (1999) 583–593. doi:10.1007/s100510050725.

- [39] S.R. Tabaei, J.-H. Choi, G. Haw Zan, V.P. Zhdanov, et al., Solvent-Assisted Lipid Bilayer Formation on Silicon Dioxide and Gold, *Langmuir*. 30 (2014) 10363–10373. doi:10.1021/la501534f.
- [40] K. Sugihara, B. Jang, M. Schneider, J. Vörös, et al., A universal method for planar lipid bilayer formation by freeze and thaw, *Soft Matter*. 8 (2012) 5525. doi:10.1039/c2sm25148e.
- [41] A.A. Brian, H.M. McConnell, Allogeneic stimulation of cytotoxic T cells by supported planar membranes., *Proc. Natl. Acad. Sci. U. S. A.* 81 (1984) 6159–63. doi:10.1073/pnas.81.19.6159.
- [42] E. Kalb, S. Frey, L.K. Tamm, Formation of supported planar bilayers by fusion of vesicles to supported phospholipid monolayers, *Biochim. Biophys. Acta - Biomembr.* 1103 (1992) 307–316. doi:10.1016/0005-2736(92)90101-Q.
- [43] J. Carter, V.A. Saunders, *Virology: principles and applications*, John Wiley & Sons, 2007.
- [44] P.S. Moore, Y. Chang, Why do viruses cause cancer? Highlights of the first century of human tumour virology, *Nat. Rev. Cancer*. 10 (2010) 878–889. doi:10.1038/nrc2961.
- [45] K.J. Looker, A.S. Magaret, M.T. May, K.M.E. Turner, et al., Global and regional estimates of prevalent and incident herpes simplex virus type 1 infections in 2012, *PLoS One*. 10 (2015) 1–17. doi:10.1371/journal.pone.0140765.
- [46] P.G. Spear, Herpes simplex virus: receptors and ligands for cell entry, *Cell. Microbiol.* 6 (2004) 401–410. doi:10.1111/j.1462-5822.2004.00389.x.
- [47] D. Shukla, P.G. Spear, Herpesviruses and heparan sulfate: an intimate relationship in aid of viral entry, *J. Clin. Invest.* 108 (2001) 503–510. doi:10.1172/JCI200113799.
- [48] R.W. Clarke, A. Drews, H. Browne, D. Klenerman, A single gD glycoprotein can mediate infection by herpes simplex virus, *J. Am. Chem. Soc.* 135 (2013) 11175–11180. doi:10.1021/ja4038406.
- [49] J.B. Lee, K. Zhang, Y.Y.C. Tam, Y.K. Tam, et al., Lipid nanoparticle siRNA systems for silencing the androgen receptor in human prostate cancer in vivo, *Int. J. Cancer*. 131 (2012) E781–E790. doi:10.1002/ijc.27361.
- [50] M. Yáñez-Mó, P.R.M. Siljander, Z. Andreu, A. Bedina Zavec, et al., Biological properties of extracellular vesicles and their physiological functions, *J. Extracell. Vesicles*. 4 (2015) 27066. doi:10.3402/jev.v4.27066.
- [51] D. Maiolo, L. Paolini, G. Di Noto, A. Zendrini, et al., Colorimetric Nanoplasmonic Assay To Determine Purity and Titrate Extracellular Vesicles, *Anal. Chem.* 87 (2015) 4168–4176. doi:10.1021/ac504861d.
- [52] S. Pant, H. Hilton, M.E. Burczynski, The multifaceted exosome: Biogenesis, role in normal and aberrant cellular function, and frontiers for pharmacological and biomarker opportunities, *Biochem. Pharmacol.* 83 (2012) 1484–1494. doi:10.1016/j.bcp.2011.12.037.
- [53] H. Valadi, K. Ekström, A. Bossios, M. Sjöstrand, et al., Exosome-mediated transfer of mRNAs and microRNAs is a novel mechanism of genetic exchange between cells, *Nat. Cell Biol.* 9 (2007) 654–659. doi:10.1038/ncb1596.
- [54] R. Friedrich, S. Block, M. Alizadehheidari, S. Heider, et al., A nano flow cytometer for single lipid vesicle analysis, *Lab Chip*. 17 (2017) 830–841. doi:10.1039/C6LC01302C.
- [55] L. Barile, G. Vassalli, Exosomes: Therapy delivery tools and biomarkers of diseases, *Pharmacol. Ther.* 174 (2017) 63–78. doi:10.1016/j.pharmthera.2017.02.020.
- [56] H. Pace, L. Simonsson Nyström, A. Gunnarsson, E. Eck, et al., Preserved Transmembrane Protein Mobility in Polymer-Supported Lipid Bilayers Derived from Cell Membranes, *Anal. Chem.* 87 (2015) 9194–9203. doi:10.1021/acs.analchem.5b01449.

- [57] C.E. Dodd, B.R.G. Johnson, L.J.C. Jeuken, T.D.H. Bugg, et al., Native E. coli inner membrane incorporation in solid-supported lipid bilayer membranes, *Biointerphases*. 3 (2008) FA59-FA67. doi:10.1116/1.2896113.
- [58] C. Théry, L. Zitvogel, S. Amigorena, Exosomes: composition, biogenesis and function., *Nat. Rev. Immunol.* 2 (2002) 569–79. doi:10.1038/nri855.
- [59] E. Van Der Pol, A.G. Hoekstra, A. Sturk, C. Otto, et al., Optical and non-optical methods for detection and characterization of microparticles and exosomes, *J. Thromb. Haemost.* 8 (2010) 2596–2607. doi:10.1111/j.1538-7836.2010.04074.x.
- [60] M. Adrian, J. Dubochet, J. Lepault, A.W. McDowell, Cryo-electron microscopy of viruses, *Nature*. 308 (1984) 32–36. doi:10.1038/308032a0.
- [61] J. Dubochet, M. Adrian, J.-J. Chang, J.-C. Homo, et al., Cryo-electron microscopy of vitrified specimens, *Q. Rev. Biophys.* 21 (1988) 129–228.
- [62] M. Almgren, K. Edwards, G. Karlsson, Cryo transmission electron microscopy of liposomes and related structures, *Colloids Surfaces A Physicochem. Eng. Asp.* 174 (2000) 3–21. doi:10.1016/S0927-7757(00)00516-1.
- [63] Y. Yuana, R.I. Koning, M.E. Kuil, P.C.N. Rensen, et al., Cryo-electron microscopy of extracellular vesicles in fresh plasma, *J. Extracell. Vesicles*. 2 (2013) 21494. doi:10.3402/jev.v2i0.21494.
- [64] N. Arraud, R. Linares, S. Tan, C. Gounou, et al., Extracellular vesicles from blood plasma: determination of their morphology, size, phenotype and concentration, *J. Thromb. Haemost.* 12 (2014) 614–627. doi:10.1111/jth.12554.
- [65] U. Erdbrügger, J. Lannigan, Analytical challenges of extracellular vesicle detection: A comparison of different techniques, *Cytom. Part A*. 89 (2016) 123–134. doi:10.1002/cyto.a.22795.
- [66] R.F. Thompson, M. Walker, C.A. Siebert, S.P. Muench, et al., An introduction to sample preparation and imaging by cryo-electron microscopy for structural biology, *Methods*. 100 (2016) 3–15. doi:10.1016/j.ymeth.2016.02.017.
- [67] C. Gardiner, D. Di Vizio, S. Sahoo, C. Théry, et al., Techniques used for the isolation and characterization of extracellular vesicles: Results of a worldwide survey, *J. Extracell. Vesicles*. 5 (2016). doi:10.3402/jev.v5.32945.
- [68] A. Adan, G. Alizada, Y. Kiraz, Y. Baran, et al., Flow cytometry: basic principles and applications, *Crit. Rev. Biotechnol.* 37 (2017) 163–176. doi:10.3109/07388551.2015.1128876.
- [69] V. Shpacovitch, R. Hergenröder, Optical and surface plasmonic approaches to characterize extracellular vesicles. A review, *Anal. Chim. Acta*. 1005 (2018) 1–15. doi:10.1016/j.aca.2017.11.066.
- [70] E. van der Pol, F.A.W. Coumans, A.E. Grootemaat, C. Gardiner, et al., Particle size distribution of exosomes and microvesicles determined by transmission electron microscopy, flow cytometry, nanoparticle tracking analysis, and resistive pulse sensing, *J. Thromb. Haemost.* 12 (2014) 1182–1192. doi:10.1111/jth.12602.
- [71] N.A. Clark, J.H. Lunacek, G.B. Benedek, A Study of Brownian Motion Using Light Scattering, *Am. J. Phys.* 38 (1970) 575–585. doi:10.1119/1.1976408.
- [72] M. Kaszuba, D. McKnight, M.T. Connah, F.K. McNeil-Watson, et al., Measuring sub nanometre sizes using dynamic light scattering, *J. Nanoparticle Res.* 10 (2008) 823–829. doi:10.1007/s11051-007-9317-4.
- [73] J. Stetefeld, S.A. McKenna, T.R. Patel, Dynamic light scattering: a practical guide and applications in biomedical sciences, *Biophys. Rev.* 8 (2016) 409–427. doi:10.1007/s12551-016-0218-6.
- [74] Z. Szakács, T. Mészáros, M.I. de Jonge, R.E. Gyurcsányi, Selective counting and sizing of single virus particles using fluorescent aptamer-based nanoparticle tracking analysis,

- Nanoscale. 10 (2018) 13942–13948. doi:10.1039/C8NR01310A.
- [75] R.A. Dragovic, C. Gardiner, A.S. Brooks, D.S. Tannetta, et al., Sizing and phenotyping of cellular vesicles using Nanoparticle Tracking Analysis, *Nanomedicine Nanotechnology, Biol. Med.* 7 (2011) 780–788. doi:10.1016/j.nano.2011.04.003.
- [76] R. Carr, Optical detection and analysis of sub-micron particles, US6280960B1, 2001.
- [77] J.R. Lakowicz, ed., *Principles of Fluorescence Spectroscopy*, Springer US, Boston, MA, 2006. doi:10.1007/978-0-387-46312-4.
- [78] A. Jablonski, Efficiency of Anti-Stokes Fluorescence in Dyes, *Nature*. 131 (1933) 839–840. doi:10.1038/131839b0.
- [79] D. Evanko, A. Heinrichs, C.K. Rosenthal, Milestones in light microscopy, *Nat. Cell Biol.* 11 (2009) 1165–1165. doi:10.1038/ncb1009-1165.
- [80] M. Minsky, *Microscopy Apparatus*, 1961. <http://www.freepatentsonline.com/3013467.html>.
- [81] M. Minsky, Memoir on inventing the confocal scanning microscope, *Scanning*. 10 (1988) 128–138. doi:10.1002/sca.4950100403.
- [82] S.W. Hell, J. Wichmann, Breaking the diffraction resolution limit by stimulated emission: stimulated-emission-depletion fluorescence microscopy, *Opt. Lett.* 19 (1994) 780. doi:10.1364/OL.19.000780.
- [83] D. Axelrod, Cell-substrate contacts illuminated by total internal reflection fluorescence, *J. Cell Biol.* 89 (1981) 141–145. doi:10.1083/jcb.89.1.141.
- [84] D. Axelrod, Total Internal Reflection Fluorescence, *Annu. Rev. Biophys. Biomol. Struct.* 13 (1984) 247–268. doi:10.1146/annurev.biophys.13.1.247.
- [85] C. Gell, M. Berndt, J. Enderlein, S. Diez, TIRF microscopy evanescent field calibration using tilted fluorescent microtubules, *J. Microsc.* 234 (2009) 38–46. doi:10.1111/j.1365-2818.2009.03147.x.
- [86] M.G. Honig, R.I. Hume, Fluorescent carbocyanine dyes allow living neurons of identified origin to be studied in long-term cultures, *J. Cell Biol.* 103 (1986) 171–187. doi:10.1083/jcb.103.1.171.
- [87] M.G. Honig, R.I. Hume, Dil and DiO: versatile fluorescent dyes for neuronal labelling and pathway tracing, *Trends Neurosci.* 12 (1989) 333–341. doi:10.1016/0166-2236(89)90040-4.
- [88] G.M. Whitesides, The origins and the future of microfluidics., *Nature*. 442 (2006) 368–73. doi:10.1038/nature05058.
- [89] Y. Xia, G. Whitesides, Soft lithography, *Annu. Rev. Mater. Sci.* 28 (1998) 153–184. doi:10.1146/annurev.matsci.28.1.153.
- [90] A. Einstein, Über die von der molekularkinetischen Theorie der Wärme geforderte Bewegung von in ruhenden Flüssigkeiten suspendierten Teilchen, *Ann. Phys.* 322 (1905) 549–560. doi:10.1002/andp.19053220806.
- [91] H. Qian, M.P. Sheetz, E.L. Elson, Single particle tracking. Analysis of diffusion and flow in two-dimensional systems, *Biophys. J.* 60 (1991) 910–921. doi:10.1016/S0006-3495(91)82125-7.
- [92] J.C. Crocker, D.G. Grier, *Methods of Digital Video Microscopy for Colloidal Studies*, *J. Colloid Interface Sci.* 179 (1996) 298–310. doi:10.1006/jcis.1996.0217.
- [93] X. Michalet, Mean square displacement analysis of single-particle trajectories with localization error: Brownian motion in an isotropic medium, *Phys. Rev. E.* 82 (2010) 041914. doi:10.1103/PhysRevE.82.041914.
- [94] C. Haiden, T. Wopelka, M. Jech, F. Keplinger, et al., Sizing of Metallic Nanoparticles Confined to a Microfluidic Film Applying Dark-Field Particle Tracking, *Langmuir*. 30 (2014) 9607–9615. doi:10.1021/la5016675.
- [95] W. Sutherland, LXXV. A dynamical theory of diffusion for non-electrolytes and the

- molecular mass of albumin, London, Edinburgh, Dublin Philos. Mag. J. Sci. 9 (1905) 781–785. doi:10.1080/14786440509463331.
- [96] M. von Smoluchowski, Zur kinetischen Theorie der Brownschen Molekularbewegung und der Suspensionen, *Ann. Phys.* 326 (1906) 756–780. doi:10.1002/andp.19063261405.
- [97] G.E. Uhlenbeck, L.S. Ornstein, On the Theory of the Brownian Motion, *Phys. Rev.* 36 (1930) 823–841. doi:10.1103/PhysRev.36.823.
- [98] G.G. Stokes, On the effect of the internal friction of fluids on the motion of pendulums, Pitt Press Cambridge, 1851.
- [99] V. Filipe, A. Hawe, W. Jiskoot, Critical evaluation of nanoparticle tracking analysis (NTA) by NanoSight for the measurement of nanoparticles and protein aggregates, *Pharm. Res.* 27 (2010) 796–810. doi:10.1007/s11095-010-0073-2.
- [100] D.T. Yang, X. Lu, Y. Fan, R.M. Murphy, Evaluation of nanoparticle tracking for characterization of fibrillar protein aggregates, *AIChE J.* 60 (2014) 1236–1244. doi:10.1002/aic.14349.
- [101] P. Jönsson, J.P. Beech, J.O. Tegenfeldt, F. Höök, Shear-Driven Motion of Supported Lipid Bilayers in Microfluidic Channels, *J. Am. Chem. Soc.* 131 (2009) 5294–5297. doi:10.1021/ja809987b.
- [102] M.A. Day, The no-slip condition of fluid dynamics, *Erkenntnis.* 33 (1990) 285–296. doi:10.1007/BF00717588.
- [103] A.J. Goldman, R.G. Cox, H. Brenner, Slow viscous motion of a sphere parallel to a plane wall—II Couette flow, *Chem. Eng. Sci.* 22 (1967) 653–660. doi:10.1016/0009-2509(67)80048-4.
- [104] M.E. O’Neill, A sphere in contact with a plane wall in a slow linear shear flow, *Chem. Eng. Sci.* 23 (1968) 1293–1298. doi:10.1016/0009-2509(68)89039-6.
- [105] M. Chaoui, F. Feuillebois, Creeping flow around a sphere in a shear flow close to a wall, *Q. J. Mech. Appl. Math.* 56 (2003) 381–410. doi:10.1093/qjmam/56.3.381.
- [106] E. Bonaccorso, M. Kappl, H.-J. Butt, Hydrodynamic Force Measurements: Boundary Slip of Water on Hydrophilic Surfaces and Electrokinetic Effects, *Phys. Rev. Lett.* 88 (2002) 076103. doi:10.1103/PhysRevLett.88.076103.
- [107] C.-H. Choi, K.J.A. Westin, K.S. Breuer, Apparent slip flows in hydrophilic and hydrophobic microchannels, *Phys. Fluids.* 15 (2003) 2897. doi:10.1063/1.1605425.
- [108] B. Cross, A. Steinberger, C. Cottin-Bizonne, J.-P. Rieu, et al., Boundary flow of water on supported phospholipid films, *Europhys. Lett.* 73 (2006) 390–395. doi:10.1209/epl/i2005-10416-4.
- [109] E. Lauga, M. Brenner, H. Stone, Microfluidics: The No-Slip Boundary Condition, in: C. Tropea, A.L. Yarin, J.F. Foss (Eds.), *Springer Handb. Exp. Fluid Mech.*, Springer Berlin Heidelberg, Berlin, Heidelberg, 2007: pp. 1219–1240. doi:10.1007/978-3-540-30299-5_19.
- [110] T. Olsson, V.P. Zhdanov, F. Höök, Total internal reflection fluorescence microscopy for determination of size of individual immobilized vesicles: Theory and experiment, *J. Appl. Phys.* 118 (2015) 064702. doi:10.1063/1.4928083.
- [111] V.P. Zhdanov, C.A. Keller, K. Glasmästar, B. Kasemo, Simulation of adsorption kinetics of lipid vesicles, *J. Chem. Phys.* 112 (2000) 900–909. doi:10.1063/1.480617.
- [112] J. Andrecka, K.M. Spillane, J. Ortega-Arroyo, P. Kukura, Direct observation and control of Supported lipid bilayer formation with interferometric scattering Microscopy, *ACS Nano.* 7 (2013) 10662–10670. doi:10.1021/nm403367c.
- [113] K. Dimitrievski, Deformation of Adsorbed Lipid Vesicles as a Function of Vesicle Size, *Langmuir.* 26 (2010) 3008–3011. doi:10.1021/la904743d.
- [114] H.-L. Wu, P. Chen, C. Chi, H.-K. Tsao, et al., Vesicle deposition on hydrophilic solid

- surfaces, *Soft Matter*. 9 (2013) 1908–1919. doi:10.1039/C2SM27450G.
- [115] V.P. Zhdanov, Mechanism of rupture of single adsorbed vesicles, *Chem. Phys. Lett.* 641 (2015) 20–22. doi:10.1016/j.cplett.2015.10.053.
- [116] D. Stroumpoulis, A. Parra, M. Tirrell, A kinetic study of vesicle fusion on silicon dioxide surfaces by ellipsometry, *AIChE J.* 52 (2006) 2931–2937. doi:10.1002/aic.10914.
- [117] K.L. Weirich, J.N. Israelachvili, D.K. Fygenson, Bilayer Edges Catalyze Supported Lipid Bilayer Formation, *Biophys. J.* 98 (2010) 85–92. doi:10.1016/j.bpj.2009.09.050.
- [118] P. Plunkett, B. a. Camley, K.L. Weirich, J.N. Israelachvili, et al., Simulation of edge facilitated adsorption and critical concentration induced rupture of vesicles at a surface, *Soft Matter*. 9 (2013) 8420. doi:10.1039/c3sm50443c.
- [119] J. Rädler, H. Strey, E. Sackmann, Phenomenology and kinetics of lipid bilayer spreading on hydrophilic surfaces, *Langmuir*. (1995) 4539–4548. <http://pubs.acs.org/doi/abs/10.1021/la00011a058> (accessed August 20, 2014).
- [120] J. Nissen, S. Gritsch, G. Wiegand, J.O. Rädler, Wetting of phospholipid membranes on hydrophilic surfaces - Concepts towards self-healing membranes, *Eur. Phys. J. B.* 10 (1999) 335–344. doi:10.1007/s100510050862.
- [121] I. Czolkos, Y. Erkan, P. Dommersnes, A. Jesorka, et al., Controlled formation and mixing of two-dimensional fluids., *Nano Lett.* 7 (2007) 1980–4. doi:10.1021/nl070726u.
- [122] G.P.H. Dietz, M. Bähr, Delivery of bioactive molecules into the cell: the Trojan horse approach, *Mol. Cell. Neurosci.* 27 (2004) 85–131. doi:10.1016/j.mcn.2004.03.005.
- [123] S. Block, V.P. Zhdanov, F. Höök, Quantification of Multivalent Interactions by Tracking Single Biological Nanoparticle Mobility on a Lipid Membrane, *Nano Lett.* 16 (2016) 4382–4390. doi:10.1021/acs.nanolett.6b01511.
- [124] P. Dechadilok, W.M. Deen, Hindrance Factors for Diffusion and Convection in Pores, *Ind. Eng. Chem. Res.* 45 (2006) 6953–6959. doi:10.1021/ie051387n.
- [125] C. Beyer, D.S. Pisetsky, The role of microparticles in the pathogenesis of rheumatic diseases, *Nat. Rev. Rheumatol.* 6 (2010) 21–29. doi:10.1038/nrrheum.2009.229.
- [126] D.L.M. Rupert, C. Lässer, M. Eldh, S. Block, et al., Determination of Exosome Concentration in Solution Using Surface Plasmon Resonance Spectroscopy, *Anal. Chem.* 86 (2014) 5929–5936. doi:10.1021/ac500931f.
- [127] H. Matsuda, Zur theorie der stationären strom-spannungs-kurven von redox-elektrodenreaktionen in hydrodynamischer voltammetrie, *J. Electroanal. Chem. Interfacial Electrochem.* 15 (1967) 325–336. doi:10.1016/0022-0728(67)85042-3.
- [128] S. Sjoelander, C. Urbaniczky, Integrated fluid handling system for biomolecular interaction analysis, *Anal. Chem.* 63 (1991) 2338–2345. doi:10.1021/ac00020a025.
- [129] R. Karlsson, H. Roos, L. Fägerstam, B. Persson, Kinetic and Concentration Analysis Using BIA Technology, *Methods.* 6 (1994) 99–110. doi:10.1006/meth.1994.1013.
- [130] L. Sercombe, T. Veerati, F. Moheimani, S.Y. Wu, et al., Advances and Challenges of Liposome Assisted Drug Delivery, *Front. Pharmacol.* 6 (2015) 1–13. doi:10.3389/fphar.2015.00286.
- [131] K.B. Johnsen, J.M. Gudbergsson, M.N. Skov, L. Pilgaard, et al., A comprehensive overview of exosomes as drug delivery vehicles - Endogenous nanocarriers for targeted cancer therapy, *Biochim. Biophys. Acta - Rev. Cancer.* 1846 (2014) 75–87. doi:10.1016/j.bbcan.2014.04.005.
- [132] X. Luan, K. Sansanaphongpricha, I. Myers, H. Chen, et al., Engineering exosomes as refined biological nanoplatforams for drug delivery, *Acta Pharmacol. Sin.* 38 (2017) 754–763. doi:10.1038/aps.2017.12.
- [133] I. SLOWING, J. VIVEROESCOTO, C. WU, V. LIN, Mesoporous silica nanoparticles as controlled release drug delivery and gene transfection carriers☆, *Adv. Drug Deliv. Rev.* 60 (2008) 1278–1288. doi:10.1016/j.addr.2008.03.012.

- [134] J. Liu, A. Stace-Naughton, X. Jiang, C.J. Brinker, Porous Nanoparticle Supported Lipid Bilayers (Protocells) as Delivery Vehicles, *J. Am. Chem. Soc.* 131 (2009) 1354–1355. doi:10.1021/ja808018y.
- [135] J.M. Chan, L. Zhang, K.P. Yuet, G. Liao, et al., PLGA–lecithin–PEG core–shell nanoparticles for controlled drug delivery, *Biomaterials*. 30 (2009) 1627–1634. doi:10.1016/j.biomaterials.2008.12.013.